Modulation of Lateral Transport by Submesoscale Flows and Inertia Gravity Waves

Anirban Sinha[1]**, Dhruv Balwada**[2]**, Nathaniel Tarshish**[3]**and Ryan Abernathey**[4]

[1]Applied Physics and Applied Mathematics Department, Columbia University, NY 10027.

[2]Courant Institute of Mathematical Sciences, New York University, NY 10012.

[3]Atmospheric and Oceanic Sciences Program, Princeton University, Princeton, NJ 08540.

[4]Department of Earth and Environmental Sciences, Columbia University, NY 10027.

Key Points:

- Lagrangian particle dispersion is enhanced by smaller scale flow features.

- Lagrangian coherent structures are eroded in the presence of submesoscales and waves.

- Satellite derived velocities may over estimate the coherence of oceanic eddies.

Corresponding author: Anirban Sinha, `as4479@columbia.edu`

Abstract

We investigate of the role of small-scale, high-frequency motions on lateral transport in the ocean, by using velocity fields and particle trajectories from an ocean general circulation model (MITgcm-LLC4320) that permits submesoscale flows, inertia-gravity waves and tides. Temporal averaging/filtering removes most of the submesoscale turbulence, inertia-gravity waves and tides, resulting in a largely geostrophic flow, with a rapid drop off in energy at scales smaller than the mesoscales. We advect two types of Lagrangian particles, (a) 2D particles (surface restricted), and (b) 3D particles (advected in full 3 dimensions) with the filtered and unfiltered velocities and calculate Lagrangian diagnostics. At large length/time scales, Lagrangian diffusivity is comparable for filtered and unfiltered velocities, while at short scales, unfiltered velocities disperse particles much faster. We also calculate diagnostics of Lagrangian Coherent Structures : rotationally coherent Lagrangian Vortices detected from closed contours of the Lagrangian-averaged Vorticity deviation and material transport barriers formed by ridges of maximum Finite time Lyapunov Exponent. For temporally filtered velocities, we observe strong material coherence, which breaks down when the level of temporal filtering is reduced/removed, due to vigorous small scale mixing. In addition, for the lowest temporal resolution, the the 3D particles experience very little vertical motion, suggesting that degrading temporal resolution greatly reduces vertical advection by high frequency motions. Our study suggests that Lagrangian diagnostics based on satellite-derived surface geostrophic velocity fields, even with higher spatial resolutions as in the upcoming SWOT mission, may overestimate the presence of coherent structures and underestimate dispersion.

Plain Language Summary

Coherent structures represent the skeleton of fluid flow in the ocean, around which the large-scale transport of material gets organized. They usually manifest as (a) material trapping vortices that transport pollutants or biogeochemical tracers over long distances or (b) ridges of material transport barriers formed by regions of high fluid stretching. In this study, we investigate the role of small-scale/high-frequency motions on coherent structures, and more generally lateral transport in the ocean, by using velocity fields generated by a high resolution ocean model. We average over the high resolution velocity fields in time to smooth out the small-scale turbulent motions and use both the smoothed and un-smoothed velocities to advect virtual particles. For temporally smoothed velocity fields, we observe strong material coherence, which breaks down when the level of temporal smoothing is reduced/removed, as the high frequency velocities scatter particles much faster. In addition, for the highest temporal smoothing, the particles experience very little vertical motion, suggesting that temporal resolution greatly affects vertical motion. Our study suggests that

diagnostics based on satellite-derived ocean surface currents, even with higher spatial resolutions, as in the upcoming SWOT mission, may overestimate the presence of coherent structures and underestimate small scale scattering.

1 Introduction

Lateral mixing in the upper ocean plays an important role in Earth's climate system. For instance, near-surface lateral mixing processes help determine the ocean's rate of uptake of tracers such as anthropogenic CO_2 [*Abernathey and Ferreira*, 2015; *Gnanadesikan et al.*, 2017; *Balwada et al.*, 2018]. Lateral mixing also strongly influences the global water mass distribution and overturning circulation [*Groeskamp et al.*, 2017, 2018]. Our ability to accurately model the ocean's impact on the global climate is consequently constrained by how effectively we parameterize lateral transport processes in the coarse-resolution models [*Gent and Mcwilliams*, 1990; *Gent et al.*, 1995; *Fox-Kemper et al.*, 2008; *Grooms and Zanna*, 2017; *Marshall et al.*, 2017]. In addition to influencing the large scale circulation and tracer distribution, lateral mixing also plays a major role in controlling the structure of synoptic oceanographic processes such as pollutant dispersal on the surface ocean [e.g. oil spills and plastics *Mariano et al.*, 2011; *Van Sebille et al.*, 2012] and local phytoplankton bloom evolution [*Mahadevan and Campbell*, 2002; *Martin*, 2003; *Mahadevan*, 2016].

Methods for characterizing lateral mixing and stirring in the ocean can be categorized broadly into two groups: analysis of spatial and temporal averages of dispersal [*Okubo*, 1971; *Zhurbas and Oh*, 2004; *Rypina et al.*, 2012; *Abernathey and Marshall*, 2013; *Roach et al.*, 2016, 2018], and identification of individual kinematic coherent flow features that might play a special role in transport. Absolute dispersion, relative dispersion, eddy diffusivity, scale dependent relative diffusivities, and area-averaged finite scale lyapunov exponents are some of the commonly used metrics in the first category [see review by *LaCasce*, 2008]. The later category is mostly falls under the umbrella of Lagrangian Coherent Structures [LCS; see review by *Haller*, 2015]. Spatial maps of finite-time Lyapunov exponents [FTLE; *Haller and Yuan*, 2000], finite scale lyapunov exponent [FSLE; *d'Ovidio et al.*, 2009], geodesic transport barriers [*Haller and Beron-Vera*, 2013], and Lagrangian averaged vorticity deviation [LAVD; *Haller et al.*, 2016] are some of the commonly used LCS techniques. (Detailed descriptions of these diagnostics can be found in Sections 3 and 4.)

The prevailing assumption is that mesoscale ocean flows, with horizontal scales of ~ 100km and evolutionary times of months, are the dominant contributor to lateral stirring on scales relevant for the large-scale circulation and transport. Phenomenologically, the mesoscale is characterized by

distinctive coherent structures such as vortices (i.e. eddies), fronts, and filaments. The relationship between these structures and the overall mixing rate is a matter of ongoing debate. For instance, *Dong et al.* [2014] and *Zhang et al.* [2014] both proposed, based on Eulerian methods, that trapping of fluid within coherent eddies and subsequent long-range transport is a major contributor to the overall mesoscale flux of mass and tracers. On the other hand, *Wang et al.* [2016] and *Abernathey and Haller* [2017], using objective Lagrangian methods, estimated that such coherent transport is only a small fraction of the total flux, and that chaotic stirring occuring outside of eddy cores is the dominant transport mechanism. Despite their different conclusions, the studies above, and indeed a large fraction of all global-scale studies of the oceanic mesoscale, relied on satellite altimetry observations.

By enabling a global synoptic view of the mesoscale, satellite altimetry, and the associated geostrophic flow obtained by taking gradients of sea-surface height (SSH), has transformed the field of oceanography fundamentally over the past 30 years [*White*, 2018]. In particular, the AVISO gridded geostrophic velocity product [*Ducet et al.*, 2000] is ubiquitous in recent studies of near-surface lateral transport [e.g. *Abraham and Bowen*, 2002; *Waugh et al.*, 2006; *Beron-Vera et al.*, 2008; *Waugh and Abraham*, 2008; *Beron-Vera et al.*, 2008; *Abernathey and Marshall*, 2013; *Klocker and Abernathey*, 2014; *Wang et al.*, 2016; *Abernathey and Haller*, 2017]. However, a new altimetry mission, the Surface Water and Ocean Topography (SWOT) satellite, is now on the horizon [*Fu and Ferrari*, 2008]. This satellite will use a Ka-band radar interferometer to provide a high-resolution swath measurement of SSH, possibly providing useful data at spatial scales of 10 km or less [*Fjortoft et al.*, 2014]. The community is now grappling with the question of what this satellite will observe, and what might be missing from our current generation of altimeters. In addition to the mesoscale, the SWOT SSH observations are expected to include significant signals from both submesoscale flows and inertia-gravity waves. Submesoscale flows have been identified as a playing a leading order role in providing a conduit for energy transfer towards microscale dissipation and diapycnal mixing [*Capet et al.*, 2008; *D'Asaro et al.*, 2011; *McWilliams*, 2016], and are also potentially important in controlling the rate of lateral spreading [*Poje et al.*, 2014] and vertical transport [*Omand et al.*, 2015; *Klein et al.*, 2008] of tracers near the surface ocean. Inertial oscillations, tides and inertia-gravity waves (IGWs) are ubiquitous in high frequency current measurements from moored instruments and surface drifters [*Alford et al.*, 2016; *Ferrari and Wunsch*, 2009; *Elipot et al.*, 2016]. These higher frequency flows project significant amount of kinetic energy on spatial scales comparable to those of the submesoscale flows (< 50km) [*Callies et al.*, 2014; *Rocha et al.*, 2016a; *Balwada et al.*, 2016; *Bühler et al.*, 2014].

The central goal of this contribution is to understand how motions from these different dynamical regimes and timescales influence Lagrangian transport in the near-surface ocean. A related question is, how reliable are transport estimates obtained from current and future satellite altimetry missions? Several past studies have examined these questions already. *Beron-Vera* [2010] calculated FLTEs from altimetry SSH-observations as well as from a low-resolution (1/4°) and high-resolution (1/12°) HYCOM simulation. He found that the FLTE distribution and spatial pattern from the low-resolution model agreed well with the observations; however, the high resolution model exhibited significantly different FTLE distributions and finer-scale structures. The conclusion was that, while current-generation altimeters capture the large-mesoscale flow structure, quantitative estimates of trajectories and mixing rates would be improved by higher spatiotemporal resolution in the observing system. Taking a more idealized route, *Keating et al.* [2011] calculated dispersion in simple models of baroclinic turbulence and explored the dependence on the spatiotemporal sampling of the velocity fields. Lagrangian diagnostics that depend strongly on small scales, such as relative dispersion and FTLE, were found to be highly sensitive to spatial sampling. Temporal sampling error was found to have a more complicated behavior, with particle overshoot sometimes leading to scrambling of Lagrangian diagnostics. The nature of the turbulence itself (i.e. the slope of the kinetic energy wavenumber spectrum) strongly constrained the required sampling, with shallower spectra requiring more resolution. In addition to simulations, Lagrangian floats, which experience advection by the full flow, can be used to probe the limitations of satellite altimetry. For instance, *Rypina et al.* [2012] showed that the eddy diffusivity calculated from surface drifters in the North Atlantic was nearly twice of that estimated from synthetic drifters generated from satellite-altimeter-derived geostrophic velocity fields. They argued that Ekman flows alone do not explain the discrepancy, and small scale unresolved geostrophic and ageostrophic velocities might be contributing to drifter-based eddy diffusivities being higher than those estimated from satellite fields. Finally, in a more recent pair of papers, *Beron-Vera et al.* [2018] and *Olascoaga et al.* [2017] attempted to determine whether a Gulf of Mexico Loop Current eddy detected from AVISO-derived Lagrangian trajectories was truly materially coherent, given the possible presence of unresolved velocities in the AVISO product. *Beron-Vera et al.* [2018] took advantage of a data-assimilating model of the region with 1km grid spacing to produce virtual Lagrangian trajectories in the presence of a developed submesoscale field. The LAVD-based Lagrangian eddy detection method [*Haller et al.*, 2016] was applied to these trajectories to extract the boundary of a coherent mesoscale structure with approximately the same position as the one identified from AVISO data. *Olascoaga et al.* [2017] validated the existence of the same materially coherent eddy using drifters and ocean color observations.

Since the earlier studies described above were conducted, a transformative new technology has emerged: ultra-high-resolution global ocean models which resolve, at least partially, the mesoscale, the submesoscale, the tides, and the IGW continuum. In the modeling studies of *Beron-Vera* [2010] and *Keating et al.* [2011], the advecting flow was assumed to be purely geostrophic, submesoscale motions were not resolved, and no tides were present. The model used by *Beron-Vera et al.* [2018] did permit submesoscale flow, but it encompassed only the Gulf of Mexico, a region with rather unique dynamics. Here we examine the question of how different scales contribute to transport using a groundbreaking new global simulation, focusing on a much larger region which includes the Agulhas and the Antarctic Circumpolar Current. We extract the velocity field from such a model, apply different levels of filtering, and calculate a range of Lagrangian mixing and transport diagnostics. This study can thus be seen as an update to and extension of prior work by *Beron-Vera* [2010], *Rypina et al.* [2012], and *Beron-Vera et al.* [2018].

To filter out motions from different dynamical regimes: we apply *simple time averaging* to the velocity fields. Specifically, we take the raw velocity fields (sampled at hourly resolution) and average them over intervals of one day and one week. We do not explicitly apply any spatial filtering [e.g. *Aluie et al.*, 2018], although the time averaging does result in smoother velocity fields (see Sec. 3 for more details). Below are some of the reasons why we choose to examine time-averaged velocities:

1. Since different dynamical regimes (e.g. waves vs. balanced motions) are most reliably separated in time rather than in space [*Wagner and Young*, 2016], temporal filtering is a straightforward way to remove different processes from a given dataset.

2. The SWOT science team has effectively adopted the daily-averaged or 3-day-averaged flow as the "truth" signal for evaluating methods to separate balanced and unbalanced motions [*Qiu et al.*, 2016; *Wang et al.*, 2018; *Qiu et al.*, 2018].

3. Ocean model simulations commonly output time-averaged velocity fields such as daily, 5-day, or monthly averages.

4. The processing algorithms used to map along-track SSH observations to gridded maps [e.g. AVISO *Ducet et al.*, 2000] involve some temporal smoothing.

5. Time averaging is computationally tractable even with very large datasets.

Although we are motived by the relevance to SWOT and other altimetry missions, our study is *not* an observing-system simulation experiment; we have not attempted to reproduce the complex pattern of spatiotemporal sampling associated with real satellite observations. Rather, our focus is on the basic

physics, for which time averaging is the most obvious filter. We are aware that more sophisticated methods exist for filtering waves and balanced motions [e.g. *Barkan et al.*, 2017; *Shakespeare and Hogg*, 2017], but these methods are computationally infeasible for our datasets. Future studies may choose to employ the diagnostic framework described here, but with different filters on the velocity field.

In this paper, we seek to answer the following three key questions: (1) How do fast-timescale velocities (sub-daily and sub-weekly) affect near-surface lateral particle dispersion statistics? (2) How do these these motions impact Lagrangian coherent structures? (3) What is the relative effect of the fast-timescale motions on vertical transport? The paper is organized as follows. In section 2, we introduce the llc4320 simulation velocity fields and examine the frequency and horizontal wavenumber power spectral density in our region of interest. In section 3, we describe the Lagrangian Particle advection experiments used to calculate the different Lagrangian diagnostics. In section 4, we study the relative diffusivity from particle dispersion and discuss the potential implication for Lagrangian coherence. In section 5, we examine Lagrangian coherent structures via FTLE and LAVD. Section 6 summarizes the results and presents conclusions.

2 Model Domain and Power Spectra

We analyze model output from a primitive equation (PE) global ocean simulation that resolves mesoscale eddies, internal tides, inertia-gravity waves, and other hydrostatic ageostrophic flows that maybe present. The simulation analyzed here is the MIT general circulation model (MITgcm) lat-lon-polar cap 4320 (llc4320), which is the highest resolution (1/48°) run in a hierarchy of simulations[*Rocha et al.*, 2016a]. The llc4320 simulation is based on a global ocean and sea ice configuration of the MITgcm, which was run with a time step of 25 s and with 90 vertical levels. The depth-based vertical grid varies in thickness from 1m at the surface to 480m near the bottom, with a maximum model depth of 7km. (Control files and details of the high- resolution llc model setups and forcing files are available at `http://mitgcm.org/viewvc/MITgcm/MITgcm_contrib/llc_hires`.)

The model is forced at the surface with six-hourly atmospheric fields from the 0.14° European Center for Medium-Range Weather Forecasts (ECMWF) atmospheric operational model analysis, which, starting in 2011, is converted to surface fluxes using the bulk formulae of *Large and Yeager* [2004]. The model also includes atmospheric pressure forcing and tidal forcing for 16 tidal con-

stituents, which is applied to MITgcm as additional atmospheric pressure forcing. The details of the tidal forcing constituents used can be found in *Savage et al.* [2017].

This model develops a realistic tidal flow field and an inertia gravity wave (IGW) continuum that is reminiscent of the observed Garrett-Munk spectrum [*Munk*, 1981], which is thought to arise from nonlinear interactions between near-inertial waves driven by winds and internal tides generated by the interaction of the barotropic tide and topography. *Savage et al.* [2017], examining the frequency horizontal wavenumber spectra of dynamic sea surface height (SSH) variance in both HYCOM (1/12.5° and 1/25° resolutions) and MITgcm (1/12°, 1/24° and 1/48° resolutions) simulations, reported that the choice of horizontal resolution affects the strength of the IGW continuum and that over most regions the higher resolution simulations captured the observed spectra more accurately at the higher frequencies (supertidal). They further showed that there are large peaks at the diurnal and semi-diurnal frequencies in regions where diurnal and semi-diurnal tides are known to be large.

The prognostic model variables were saved at hourly intervals as instantaneous snapshots (not averages). The use of instantaneous snapshots means that very high frequency (sub-hourly) oscillations may be aliased, potentially introducing spurious motion into the Lagrangian trajectories. We have no means to quantify this effect, other than by comparing with the temporally averaged velocity fields, for which any potential aliasing is smoothed away. We extract 73 days (starting From September 13, 2011) of hourly llc4320 model output from a broad region in the South Atlantic which includes the Agulhas leakage and Antarctic Circumpolar Currents. The region spans $15.5°W$ - $29.5°E$, $57°S$ - $26.6°S$). A snapshot of the surface Kinetic Energy in the model domain is shown in Fig. 1. This region exemplifies different regimes of flow, namely strong shear flow in the ACC and coherent eddies in the Agulhas. Qualitatively, the ACC would be dominated by hyperbolic coherent structures, and the Agulhas leakage by elliptic coherent structures [*Haller*, 2015].

In the following sub-sections we examine the frequency and wavenumber kinetic energy spectra to provide a sense of the relative amplitudes of the tides, IGWs and balanced motions.

2.1 Time Averaging

As described in the introduction, we employ time averaging of the velocity fields to filter out the fast timescales associated with tides, IGWs, and submesoscale flow. This is accomplished by grouping the *hourly* snapshots into *daily* and *weekly* blocks and taking the mean. This mean is representative of the time at the midpoint of each block. We refer to the daily- and weekly-averaged velocities generically as the *filtered velocities*. These three different velocity datasets constitute

the main inputs to our analysis. The outputs are the different diagnostics described in subsequent sections.

2.2 Frequency Spectra

To assess how much energy is contained at different timescales, we calculate the rotary power spectrum of the surface velocities. The velocity is represented as complex valued time series, $\underline{u(t)} = u(t) + iv(t)$, for the 73 day period at each grid point. A Hanning window is applied to the time series before calculating the corresponding spectrum at each grid point, denoted by $\hat{u}\hat{u}^*(\omega)$, where $\hat{u}(\omega)$ is the Fourier transform of the complex valued time series, multiplied by a Hanning window. The power spectrum at each latitude is calculated by averaging the over the range of longitudes in the domain. The advantage of calculating the rotary spectrum is that the the positive and negative frequencies correspond to the counter clockwise and clockwise motions. For the purpose of frequency spectral analysis, the filtered velocities as linearly interpolated in time back to the original hourly temporal resolution, as this is how they are treated later when used for advecting Lagrangian particles.

We show the frequency power spectrum at $46.005°S$ latitude in Fig 1 as a representative, as the frequency spectra at different latitudes in the domain did not vary qualitatively. The spectrum is characterized by sharp peaks at frequencies greater than that corresponding to a day. The inertial oscillations ($\omega = \frac{f}{2\pi}$), and tides (M_2, M_4, M_6 and higher) are clearly visible. *Savage et al.* [2017] had shown that a few locations in the North Pacific, where McLane profiler observations were available, the tides in the modeled velocity time series were similar or greater in amplitude when compared to the observations.

In addition to inertial oscillations and tides, there is also a background level of power that presumably results from IGWs, and balanced and ageostrophic flows. However, the frequency decomposition does not allow us to differentiate between these. In the next section we attempt to shed some light on the dynamics of the modeled flows by performing a decomposition of the wavenumber spectrum into rotational and divergent components.

The affect of time averaging is, unsurprisingly, to attenuate the signal power strongly above the averaging frequency. Time averaging plus linear re-interpolation is clearly not a perfect filter, however; residual high-frequency peaks and valleys remain in the filtered power spectra, with valleys corresponding to harmonics of the averaging time. While these stand out clearly on the log-log plot

of Fig. 1, we note that the power level at frequencies above the averaging frequency is everywhere

smaller by at least a factor of 100 than the raw power level.

2.3 Wavenumber Spectra

In this section we investigate the wavenumber power spectra of the raw and filtered velocity

fields. Further, we decompose these spectra into horizontally non-divergent and divergent compo-

nents following a methodology described in *Bühler et al.* [2014]. The mesoscale motions in the

ocean are largely balanced/geostrophic, and hence non-divergent, while the tides, inertial oscillations

and IGWs project onto both the divergent and non-divergent parts of the horizontal flow. Subme-

soscale flows have a dominant balanced component, but at high Rossby number can have some

projection onto the divergent component too [*McWilliams*, 2016]. We also compare the effect of

the temporal filtering on the wavenumber spectra of the surface KE under the Helmholtz decompo-

sition. This helps us assess what fraction of the energy in the spectra at different scales is due to

the non-divergent/rotational (mesoscale and balanced submesoscales) and divergent (tides, inertial

oscillations, IGWs and unbalanced submesoscale) flows.

We calculate the 1D horizontal spectra along each latitude line in a subdomain spanning the

full range of longitudes as in our domain, but spanning $\sim 40°S - 50°S$ in latitude for the surface

velocity field. The top panel in Fig 3 shows the rotational (solid) and divergent (dashed) parts of the

longitudinal (zonal) and transverse (meridional) KE spectra for the hourly unfiltered velocity (blue),

daily-averaged velocities (red) and weekly-averaged (green) velocities. The thick lines represent the

meridional mean of the 1D Fourier decomposition along each latitude line from $\approx (40°S - 50°S)$,

and the shading represents the one standard deviation error. We also calculated the power spectral

density of isotropic surface KE ($E(K)$) in two smaller regions, spanning the Agulhas ($3°$ W - $15°E$,

$42° - 27°S$), and the ACC ($10°W$ - $10°W$, $54° - 42°S$) (as shown in Fig. 1) from the 2D wavenumber

spectra in these regions by integrating azimuthally over each K ($K = \sqrt{k^2 + l^2}$) in the wavenumber

space.

$$E(K) = \iint_{k^2+l^2=K^2} E(k,l)dkdl \tag{1}$$

The bottom panel in Fig. 3 shows the ratio of unfiltered to filtered isotropic power spectral density

at the surface. The red lines show the ratio of the power between hourly : weekly velocities

($E_h(K)/E_w(K)$) and the blue lines correspond to hourly : daily velocities ($E_h(K)/E_d(K)$).

The spectra are mostly flat at large scales and start dropping off at scales smaller than 200km.

The drop off in energy at length scales smaller than 10km is very rapid, presumably a result of

the viscous dissipation. In the discussion here, we restrict our attention to the 10 - 200 km range, which is influenced by the temporal filter but not strongly influenced by dissipation. We observe a consistent decrease in power with filtering in both the rotational and divergent components at length scales smaller than $\sim$ 100km. This is an indication that the high frequency motions filtered out by time averaging are primarily associated with small spatial scales. The non-divergent component of the spectra is more energetic than the divergent component, even for the unfiltered velocities. The ratio of the non-divergent to divergent energy increases with low pass filtering (top panel, upper inset, Fig. 3). The difference of the divergent KE between the hourly unfiltered and daily filtered KE is larger than the difference of divergent KE between daily and weekly filtered KE at all intermediate length scales (lower inset, top panel). This indicates that the superinertial motions have a large divergent component. The isotropic KE is 30 times lower for the weekly filtered velocities and 3 times lower for the daily filtered velocities at the smallest scales (< 10 km). This indicates that while at intermediate scales, the daily filter removes most of the divergent KE, the total KE loss is much greater going from the daily filter to the weekly filter. At the smallest scales, similar amounts of energy are lost at each successive filtering.

The spectral slope for the rotational component of the unfiltered velocity field roughly follows a k^{-3} power law in the 50-200km range, and flattens out to k^{-2} at smaller length scales. The corresponding divergent component of the unfiltered velocity follows approximately a k^{-2} at all length scales. With temporal filtering the power of the divergent component is reduced, but the spectral slope is relatively uninfluenced. However, the spectral slope of the non-divergent component of energy becomes steeper with temporal filtering, getting close to k^{-3} power law in the 10-200km range with the weekly temporal filter. This suggests that the weekly filtered velocity fields, where the influence of the fast ageostrophic flows has been removed, are smooth and might be kinematically similar to interior-QG dynamics [*Le Traon et al.*, 2008; *Keating et al.*, 2011].

3 Offline Lagrangian Particle Advection Experiments

The goal of this work is to understand the lateral transport mechanisms that are active in the surface ocean. We use numerical particles to elucidate the influence of the Eulerian flow field on the Lagrangian transport. We employ the offline mode [*Abernathey and Marshall*, 2013] of the MITgcm, where the dynamical core is disabled, and the velocity fields for our region ($15.5°W$ - $29.5°E$, $57°S$ - $26.6°S$) are taken directly from the llc4320 hourly model output to advect Lagrangian particles injected at the surface.

While many past LCS studies have relied on advecting particles with surface geostrophic velocities, we take advantage of the llc4320 model to examine the particle trajectories without the geostrophic assumption, and permitting 3D motion. We set up experiments with two kinds of particles: 2D and 3D. 2D particles are restricted to stay at the surface layer and are advected only by the horizontal component of the surface velocity, while the 3D particles are allowed to be advected by the full three dimensional velocity field. The 3D particles are most representative of the true Lagrangian trajectories, while the 2D particles can be thought of as the approximate trajectories of inertial particles whose strong buoyancy effectively constrains them to remain close to the sea surface [*Haller and Sapsis*, 2011; *Maxey and Riley*, 1983], similar to surface drifters. The 3D particles can give us some insight into the influence of the strong vertical velocities that are often seen in high resolution simulations [*Klein and Lapeyre*, 2009; *Choi et al.*, 2017] on Lagrangian transport and shed light on the limitations of assuming 2D geostrophic flow.

Table 1: Lagrangian particle advection experiments carried out

Experiment	Hourly Velocities	Daily Averaged Velocities	Weekly Averaged Velocities
3D particles	3D-h	3D-d	3D-w
2D particles	2D-h	2D-d	2D-w

Table 1 summarizes the six experiments conducted for our present study and the shorthand we will use for referring to these experiments. Here the 2D-w experiment represents the case that is closest to Lagrangian particle advection using satellite altimetry derived velocities, which have a nominal temporal resolution of 7-10 days. As noted in the introduction, none of these cases should be considered an observing-system simulation, since the sampling and processing behind real satellite altimetry products is considerably more complex than simple time averaging. If we were to arrange these experiments in order of most to least realistic, the closest to the "real" ocean would be the 3D-h case, and the least realistic, and the closest to geostrophic trajectories inferred from satellite altimetry, would be the 2D-w case, with realism decreasing downward and right in Table 1. Surface drifter experiments [*Lumpkin and Johnson*, 2013] are closest to the 2D-h case, as drifters do not track the fluid vertically.

350 In each case, the particles are initialized on a regular horizontal grid spacing of $1/100° \times 1/100°$

351 at the surface, a total of 4450×2900 particles. For each of the simulations, when a particle reaches

352 the edge of the domain, it stops moving due to the imposed boundary conditions and therefore "dies".

353 We remove the "dead" particles from the analysis that is performed in this study to ensure that all

354 trajectories used here are of the same temporal length. This effectively creates a spatial mask (seen

355 in Fig. 6) over the domain.

356 For comparison with some (but not all) diagnostics, we also computed particle trajectories in

357 the Agulhas region ($20°W$ - $30°E$, $60°S$ - $20°S$, roughly the same region as our Agulhas sector for

358 llc) from a previous MITgcm offline simulations for the entire globe. In this global offline simulation,

359 particles were initialized on a $1/32°$ horizontal grid, and had the trajectories output daily. The details

360 of the MITgcm offline simulations with AVISO velocities can be found in *Abernathey and Haller*

361 [2017].

362 In the following sections we describe the characteristics of the Lagrangian transport, using

363 relative dispersion statistics and Lagrangian coherence, that is experienced by the particles in the

364 different experiments.

4 Relative Dispersion and Diffusivity

366 Dispersion is one of the most basic metrics that can be used to quantify the influence of turbulent

367 motions on transport. Similarly to the variance, it gives a measure of the size of a group of particles.

368 Generally, dispersion is measured as either the absolute dispersion, relative to the initial release

369 point of particles, or the relative dispersion, relative to the evolving center of mass of the group

370 of particles. In the absence of a background mean flow and for Brownian/uncorrelated motion,

371 absolute dispersion and relative dispersion are the same. However, in more complex flows like in the

372 ocean, relative dispersion provides a better measure of the spread of particles by turbulence alone

373 and is not influenced by mean advection. *Babiano et al.* [1990]; *Bennett* [1984]; *LaCasce* [2008];

374 *Foussard et al.* [2017] provide excellent reviews of relative dispersion, and theoretical relationships

375 for a inertial ranges of 2D turbulent flows. Here we use relative dispersion as a measure to see how

376 the bulk transport properties change with time-averaged velocity fields.

377 Relative dispersion (D_{rel}) is defined as the mean squared separation over all particle pairs,

378 where the choice of pairs provides a conditional averaging. Here we define pairs as all particle

combinations that were initially separated by the same distance r_o.

$$D_{rel}(t, r_o) = \frac{1}{2N(N-1)} \sum_{i \neq j; |\mathbf{X}_i(0) - \mathbf{X}_j(0)| = r_o} |\mathbf{X}_i(t) - \mathbf{X}_j(t)|^2, \qquad (2)$$

where N is the number of particles, and $\mathbf{X}_i$ and $\mathbf{X}_j$ are position vectors of the two particles in the pair. A corresponding relative diffusivity, the rate of separation growth, can be defined as

$$K_{rel}(t, r_o) = \frac{1}{2} \frac{d}{dt} (D_{rel}(t, r_o)) \qquad (3)$$

We can also, albeit coarsely, relate the relative diffusivity to a length scale by replacing the time dependence by the corresponding square root of the relative dispersion,

$$K_{rel}(r, r_o) = K_{rel}(D_{rel}(t, r_o)^{\frac{1}{2}}, r_o), \qquad (4)$$

where r is the separation length scale.

Two regions—Agulhas ($3° \text{W} - 15°E$, $42° - 27°S$), and ACC ($10°\text{W} - 10°W$, $54° - 42°S$)—were chosen for calculating the relative dispersion and diffusivity from the simulations with the filtered and unfiltered velocities (as shown in Fig 1). We chose r_o to be the grid separation ($\sim$ 1km) at which all particles were initially released, as this allows the turbulent transport to sampled down to the smallest length scales in the system. Except for the differences in magnitude, the two regions exhibit qualitatively similar behavior. Therefore, unless otherwise noted, the following discussion applies equally to both regions.

In Fig. 4, the relative dispersion, the relative diffusivity and the ratios of relative diffusivities for the particles advected by the unfiltered and filtered velocities are plotted as a function of time in the two sectors. The unfiltered hourly velocities disperse particles faster and farther than the daily or weekly filtered velocities. At small time, < 5-10 days, the diffusivity calculated from the rate of change of dispersion is small, $O(100 \text{ m}^2/\text{s})$, and increases by 3-4 orders of magnitude with time for both filtered and unfiltered velocities. This increase in diffusivity can be understood as a result of the larger, more energetic eddies starting to play a more dominant role in dispersion at longer times. The smaller eddies in the unfiltered velocity fields are able to spread particles apart more rapidly than the filtered velocity fields, allowing the influence of the larger eddies to be felt sooner.

The relative diffusivity is the largest for the unfiltered hourly velocity fields. The ratio of the hourly to weekly diffusivities goes from 8 at small times to ~ 3 at the end of the simulation period ($\sim$ 60 days) in the Agulhas. In the ACC, the diffusion by hourly velocities is $3 - 5$ times higher than the weekly velocities at all times, and the relative magnitude does not decay post $\sim$ 10 days. The

absolute magnitudes of the relative diffusivity at initial times are also smaller for the ACC compared to the Agulhas region. This is an indication that the smaller eddies, which influence the dispersion initially, in the ACC are weaker or less efficient at dispersing particles than in the Agulhas. This might be due to one or both of the following reasons: (a) the scales of submesoscale might just be smaller in the ACC and so are not resolved in the llc4320 or (b) the presence of a strong mean flow suppresses the growth of the submesoscale modes [*Taylor et al.*, 2018].

It should also be noted that the difference in tracer spreading between the hourly and daily velocity fields is smaller than the difference between the hourly and weekly. This is to be expected as we damp out a larger fraction of the kinetic energy with a longer time filter (see Fig. 1). However, this is also an indication that tidal and wave motions, which are present only at time scales smaller that 1 day, are less efficient at inducing turbulent transport. Small amplitude linear waves in a homogeneous background would indeed be expected to cause zero dispersion.

An alternate perspective to the time domain is to look at the relative diffusivity as a function of separation length scale (Equation 3, Figure 5). From this perspective, the difference between the turbulent transport by hourly unfiltered and daily filtered velocity is less: the relative diffusivity due to the hourly velocity fields in only about 20-30% greater than the daily filtered velocity fields at small length scales, and almost in distinguishable at large length scales. The relative diffusivity for the weekly velocity field is about half the size of the hourly velocity field. The reason for this difference is that the mapping from $K_{rel}(t)$ to $K_{rel}(r)$ uses the dispersion D itself to define the length scale, which means that, at a given value of r, we are comparing dispersion from the different experiments at different times in the particle evolution. This collapses the distinct curves of Fig. 4 into a much tighter relationship.

This section has shown that fast-timescale motion make a considerable contribution to mixing, particularly at small scales but also at scales of hundreds of km / months. Such fast-timescales are absent from current generation altimetry-derived velocity products. Thus, in agreement with *Rypina et al.* [2012] and *Beron-Vera* [2010], we conclude that altimetry-inferred mixing diagnostics in the upper ocean may underestimate dispersion significantly. This enhanced mixing at small scales by high-frequency velocities can be explained, at least qualitatively, due to the influence of reduced KE at small length scales (seen in Figure 3). In addition, we also note that the spectral slopes are steeper in the ACC than the Agulhas region (not shown in the figures), indicating weaker overall submesoscale energy and correspondingly a relatively smaller influence on dispersion. It appears that we are likely to underestimate lateral mixing at small scales by a factor of at least 2, dependent

on the region of the ocean, if we neglect the fast timescales. A factor of 2 discrepancy was also observed [*Rypina et al.*, 2012] between diffusivity estimates from drifters and satellite altimetry in the North Atlantic.

While relative dispersion and diffusivity provide bulk estimates of differences in turbulent transport, they do not provide a detailed picture of the mechanisms at work in the dispersion of particles. Further understanding can be developed by looking at the details of the kinematics. In the subsequent sections we examine how small scales can affect Lagrangian coherence, by studying different Lagrangian coherent structure diagnostics in the presence/absence of these high frequency motions.

5 Lagrangian Coherence Diagnostics

A visual survey of the ocean mesoscale suggests the presence of structures in the flow, rather than a random diffusive transport. These structures, which often show coherent motion in space and time, are referred to as Lagrangian Coherent Structures [LCSs; see review by *Haller*, 2015]. There exist a plethora of different methods for detection of LCSs. *Hadjighasem et al.* [2017] present a very detailed summary of the various existing diagnostics in the context of idealized 2D turbulence examples. Each of these methods has its merits and drawbacks. For our study we have chosen to focus on two of these methods - Finite time Lyapunov exponents (FTLE) and Lagrangian averaged vorticity deviation (LAVD). FTLE has been around for quite some time as a method for detecting material transport barriers and is useful for detecting jets and other strong shear flows (attracting and repelling hyperbolic LCSs)[*Pierrehumbert and Yang*, 1993; *Haller*, 2002]. On the other hand, the recently devised LAVD method has been shown to be a robust, objective method for detecting materially bounded vortices (elliptic LCSs) [*Haller et al.*, 2016; *Beron-Vera et al.*, 2018]. As such, FTLEs and LAVD serve as complimentary methods for detecting different types of LCSs.

5.1 Finite Time Lyapunov Exponent

Many previous studies [*Waugh et al.*, 2006; *Waugh and Abraham*, 2008; *Keating et al.*, 2011; *Waugh et al.*, 2012; *Beron-Vera et al.*, 2008] have computed FTLEs from the advection of Lagrangian particles with ocean velocity fields. We briefly review the basic theory in the following paragraphs. Following *Haller* [2011]; *Farazmand and Haller* [2012], for Lagrangian particles initially located at (x_0, y_0) at time t_0 are advected to (X, Y) at time t, then the flow map at time t is defined by their

466   instantaneous positions as

$$\mathbf{F}_{t_0}^t(x_0, y_0) := (X(x_0, y_0, t), Y(x_0, y_0, t)) \tag{5}$$

467   From the flow map $\mathbf{F}_{t_0}^t$ we calculate the Jacobian as $\nabla \mathbf{F}_{t_0}^t(x_0, y_0)$. Then, the right Cauchy-Green

468   stress tensor $\mathbf{C}_{t_0}^t$ is calculated as

$$\mathbf{C}_{t_0}^t(x_0, y_0) = \left(\nabla \mathbf{F}_{t_0}^t(x_0, y_0)\right)^T \nabla \mathbf{F}_{t_0}^t(x_0, y_0) \tag{6}$$

469   This symmetric, positive definite tensor, $\mathbf{C}_{t_0}^t(x_0, y_0)$ admits two real positive eigenvalues, λ_i and real

470   orthogonal eigenvectors, ξ_i, defined by

$$\mathbf{C}_{t_0}^t(x_0, y_0)\xi_i = \lambda_i \xi_i, \quad \|\xi_i\| = 1, \quad i = 1, 2$$

471   and

$$0 < \lambda_1 \leq \lambda_2$$

472   where λ_i and ξ_i are functions of (x_0, y_0, t). The maximum eigenvalues of this C-G tensor, λ_2 gives

473   the forward time FTLE as follows

$$FTLE = \frac{1}{t - t_0} \log(\lambda_2). \tag{7}$$

474   For each time t, (7) provides a measure of the integrated strain along the trajectory of each particle

475   for the time period $t - t_0$ and can be plotted at the initial position (x_0, y_0) of each particle. Similarly

476   the backward time FTLE at the location $(X(x_0, y_0, t), Y(x_0, y_0, t))$ can be calculated as the negative of

477   the logarithm of the smallest eigenvalue λ_1 of $\mathbf{C}_{t_0}^t(x_0, y_0)$ at the initial position (x_0, y_0) [*Haller and*

478   *Sapsis*, 2011]. Unless otherwise mentioned we refer to the forward time FTLE, mapped at the initial

479   positions (x_0, y_0), as FTLE in this study. In Fig. 6, the FTLE after 30 days is shown for each of the

480   six experiments described in Table 1.

481   We also consider the 30 day FTLE fields, for particles advected with AVISO velocities in Fig. 7

482   (left panel) for comparison. The FTLE field shown is for the region $(15.5°W - 29°E , 56°S - 27°S$, the

483   same region as our Agulhas sector for llc). We note that although the FTLE shown for the AVISO is

484   for a 30 day period, it is not the same 30 day period, so we are not offering a direct comparison here.

485   Also, as opposed to our simulations where we had to impose boundary conditions on the limited

486   domain under consideration, the AVISO particle simulation was done on the entire globe and thus

487   does not show masked out regions corresponding to particles that left the domain.

We observe that the FTLE field from the AVISO velocities is qualitatively very similar to the FTLE field from the llc model experiments with the weekly averaged velocities. When we compare the two panels on the right of Fig. 6, with the left panel in Fig. 7, we notice the maxima of FTLE to be the same order of magnitude and distributed similarly in the domain in both these figures. In addition, the coherent patterns traced out by the high FTLE ridges have roughly the same length scales. This is not surprising, since, by filtering out timescales smaller than a week, we are effectively reducing the resolution of the llc model to that obtained from AVISO.

We start with a qualitative description of the structures observed in the FTLE maps and examine the sensitivity of FTLE to the time interval. The FTLEs (zoomed in near a coherent mesoscale eddy observed in 2Dw) at 5, 15, 30 and 60 day periods, for the three 2D experiments are shown in Fig. 8. The ridges (maxima) of FTLE represent regions of high fluid strain which may act as material transport barriers. We observe that these ridges are long, smooth and well defined only for weekly filtered velocities at long times. At short times (< 15 days), clear, well defined fine scale FTLE ridges are observed for the hourly and daily averaged velocities, revealing a strong submesoscale signature. At times longer than 30 days, for the daily velocities, we observe some coherent FTLE ridges with complex large amplitude fine scale structure. However, at such long timescales, due to vigorous mixing at small scales by the hourly velocities, the large scale patterns of FTLE traced out by the mesoscale eddy are completely engulfed by the small scale features and the FTLE field appears blurry. This finding is somewhat different from *Beron-Vera* [2010], who found that high resolution (1/12°) SSH-inferred geostrophic velocities produced FTLE fields with very intricate fine scale structure which was still discernible. Our experiments use a higher resolution model velocity fields with a strong unbalanced component, and as a result, vigorous mixing by submesoscale turbulent flows and inertia gravity waves evidently leads to complete scrambling of coherent FTLE ridges. For the weekly filtered velocities, there is little qualitative difference as the time period is changed, but the overall magnitude of the FTLE value decreases.

A useful quantitative way to assess the effect of filtering on the FTLEs is via their distributions. The PDFs of the same FTLE fields are shown in Fig. 9. For comparison, we also show the the 30 day FTLE fields from a similar region produced from AVISO surface geostrophic velocities. As discussed by *Beron-Vera* [2010], an FTLE PDF with a long tail suggests that most of the mixing in the flow is accomplished a few special regions of strong stretching (such as coherent filaments). In contrast, a more Gaussian PDF indicates that a range of structures at all scales contribute to mixing. *Beron-Vera* [2010] found that FTLEs from AVISO and those from a 1/4∘ model exhibited a very similar PDF, which peaked between 0 and 0.1, with a long tail extending to larger values.

As shown in Fig. 9, in strong contrast to the AVISO distribution, the FTLE from both the hourly and daily experiments is skewed towards high values, with peaks in the range of 0.2 - 0.3. Daily filtering shifts the distribution somewhat towards lower values, but only weekly filtering induces a qualitative change; the weekly PDF is more symmetric and peaks close to 0.1. The median FTLE value for AVISO velocities is shifted even further left than the weekly velocities. This again is in agreement with the hypothesis that satellite altimetry represents the 2D-w corner of Table 1. None of the PDFs diagnosed from our experiments displays a skewness similar to the AVISO-derived FTLE, whose PDF peaks around 0.05. This means that the mixing process in the LLC simulation is generally more intense and homogeneous. This finding is somewhat similar to *Beron-Vera* [2010], who showed that the distribution of FTLE was skewed towards higher growth rates when high resolution ($1/12°$, HYCOM) velocities (computed from SSH) were used to advect particles and towards low values when low resolution (interpolated to $1/4°$) velocities were used. In addition, at short times (< 15 days), the hourly and daily averaged FTLE distributions are markedly different from each other; however, at long times (60 days), they almost overlap.

Furthermore, vertical motion strongly affects the character of the FTLE ridges. When the fastest timescales are considered, there is significant difference between the FTLE fields between particles that are restricted to one vertical plane and particles that are advected in three dimensions. This difference is more clearly seen in the PDF of the FTLE for the 2D and 3D particles. With hourly velocities, the distribution differs markedly between 2D and 3D particles; with the 2D particles having smaller FTLE overall, and the distribution is less peaked. This difference decreases for the daily averaged velocities, and the 2D and 3D FTLE distributions are almost exactly the same for the weekly averaged velocities. This shows that, by filtering out faster timescale processes we are also filtering out vertical motions associated with these fast timescales.

FTLE tells us about strain rates in the flow field, which represents one kind of coherence, namely material transport barriers due to fluid stretching. As we get further away from the satellite altimetry (non-divergent) like velocity fields, and get closer to velocity fields with unbalanced flows (as we might expect with a more realistic representation of the ocean), we observe higher and smaller-scale strain in the domain.

In the next section, we describe the methodology used to detect materially bounded eddies (coherent Lagrangian vortices) from our Lagrangian particle advection experiments and investigate the role of temporal filtering on the presence or absence of these structures.

5.2 Lagrangian Averaged Vorticity Deviation

The role of coherent mesoscale eddies in ocean transport is currently a topic of great interest and debate. Do such eddies trap material and transport it over long ranges, without exchange with the outside environment, or are they "leaky?" Agulhas rings are perhaps the best-known example of such coherent eddies [*Van Sebille et al.*, 2012], which partly motivated the choice of our study region. In the following paragraphs, we describe a method for objectively detecting such coherent vortices and then describe how this method was applied to the LLC velocity dataset.

There have been numerous Eulerian and Lagrangian techniques developed to attempt identify coherent mesoscale eddies [e.g. *Isern-Fontanet et al.*, 2006; *Chelton et al.*, 2007; *Beron-Vera et al.*, 2013; *Haller and Yuan*, 2000; *Haller*, 2002; *Haller and Beron-Vera*, 2013; *Haller et al.*, 2016]. Here we apply the recently developed method of *Haller et al.* [2016] based on Lagrangian-averaged vorticity. The physical essence of this method is that it searches for compact regions of the fluid which experience similar rotation over their lifetime—this definition fits well with most oceanographers' intuitive understanding of a vortex or eddy.

Our method and numerical approach to identifying such eddies is identical to the one described in *Abernathey and Haller* [2017]. We begin with the instantaneous two-dimensional relative vorticity ζ, defined by

$$\zeta = -\frac{\partial u}{\partial y} + \frac{\partial v}{\partial x} \ . \tag{8}$$

In our experiments, the vorticity is calculated from the input velocity fields and interpolated linearly in space and time to the positions of all the Lagrangian particles. To maintain the frame-invariance of the method [*Haller et al.*, 2016], it is necessary to remove any solid body rotation. For that purpose, the vorticity deviation is obtained by subtracting the spatial mean vorticity (denoted by $\langle \cdot \rangle$): $\zeta'(x, y, t) = \zeta(x, y, t) - \langle \zeta \rangle (t)$. The Lagrangian Averaged Vorticity Deviation (LAVD) is then defined as the average of the instantaneous Lagrangian vorticity (ζ') along the flow trajectory [*Haller et al.*, 2016; *Abernathey and Haller*, 2017]:

$$LAVD_{t_0}^{t_1}(x_0, y_0) = \frac{1}{t_1 - t_0} \int_{t_0}^{t_1} |\zeta'(X(x_0, y_0, t), Y(x_0, y_0, t), t)| \, dt \tag{9}$$

where X, Y is the Lagrangian position of the particle initial released at point x_0, y_0. Thus, the LAVD is a function of initial position (x_0, y_0) and also the time interval t_0, t_1. In Fig. 10, the LAVD, integrated for 30 days, is shown for all 6 experiments. For comparison, we also show the the 30 day LAVD fields from a similar region produced from AVISO surface geostrophic velocities in Fig. 9 (right panel).

581   Coherent vortices can be thought of as collectively rotating fluid that is organized into concentric

582   bands around a rotating near-circular core. In our study, this is represented by a family of closed

583   LAVD contours surrounding an innermost LAVD maximum (grey contours in Fig. 12). The outer

584   boundary of the rotationally coherent Lagrangian vortex (RCLV) is determined by a threshold on the

585   convexity of the contour [*Haller et al.*, 2016]. For this purpose, we utilize the convexity deficiency

586   (CD), as a measure of the convexity of a 2D LAVD contour. This is the primary tuning parameter

587   of the LAVD method. CD is defined as the difference in area enclosed by the contour and its convex

588   hull divided by the area enclosed by the contour. Once a local maximum of LAVD is detected, we

589   move outwards from this maximum across the LAVD contours using a bisection search algorithm

590   until we hit the outermost contour with the target CD. The method does not discriminate between

591   cyclonic or anticyclonic vortices, since absolute values of vorticity are used for the definition.

592   The procedure is implemented using the `scikit-image` package in Python [*van der Walt et al.*,

593   2014]. The different tuning parameters for this algorithm are CD, the minimum area (in pixels) of

594   the RCLV and the minimum distance between the center of two RCLVs. Details of the numerical

595   computation and the choice of tuning parameters can be found in *Haller et al.* [2016]; *Abernathey*

596   *and Haller* [2017]; *Tarshish et al.* [2018], (`https://github.com/rabernat/floater`). The

597   coherency and population of the identified RCLVs are acutely sensitive to CD, as can be seen in

598   Fig. 11.

599   In Fig. 11, we plot the number of RCLVs detected for each choice of CD for all our 2D particle

600   experiments. For the 2D cases, we identify RCLVs at long time for the daily and hourly velocities

601   only when we relax the CD to very large values (≥ 0.05) and set the minimum area and the minimum

602   distance between RCLVS to very small values ($\approx 200\ km^2$ and $\approx 50\ km$, respectively). We observe

603   very convex coherent vortices ($CD < 0.05$) only for weekly averaged velocities. For the hourly and

604   daily averaged velocities, there are no coherent eddies to identified at low values of CD.

605   How does CD affect the character of the identified RCLVs? In Fig. 12, we show the outermost

606   LAVD contours for each particular choice of CD for one of the prominent RCLVs detected from the

607   2Dw case and show the initial and final positions of the particles inside this RCLV for each choice

608   of CD in Fig. 13. These two figures show that, if we choose a large CD (0.25), the boundary of

609   the RCLV becomes less defined and exhibits extreme filamentation, and for a low CD (0.001), the

610   permitted RCLV is very small ($\approx 100 km^2$). So we settle on 0.1 to be an optimum choice for CD

611   for our study. For this particular choice of CD, with more conservative choices of minimum area

612   ($> 400 km^2$) and minimum distance ($> 100 km$), we only detect about 10 - 20 RCLVs for the 2D-w

and 3D-w cases and none for the rest of the cases. For smaller choices of CD, most of the RCLVs are very small and/or short lived. So while we detect many RCLVs when the particles are advected with weekly averaged velocities, for the same choice of parameters, the algorithm does not detect large/ long-lived coherent vortices for small enough choice of CD.

5.3 Case Studies of a few Coherent Vortices

The analysis above shows that only the weekly-averaged velocities produce substantial numbers of RCLVs. In order to determine what causes this breakdown of coherence for daily and hourly velocities, when we travel diagonally from 2D-w to 3D-h in Table 1, selecting a few of the relatively large and long-lived RCLVs detected from the 2D-w case and compare the 3D trajectories of those particles with the same initial positions for the three cases—3D-w, 3D-d and 3D-h—at different times. Fig. 14 shows the evolution of two such RCLVS (represented by the colors, red and green) over 5, 15, 30 and 60 days. The left panels show the initial positions of particles inside 2 RCLVs detected from closed convex contours ($CD = 0.1$) of LAVD from the 2D-w simulation. The top two rows show the horizontal and vertical positions of the particles inside the RCLV at different times in the 3D-w case. The middle two rows correspond to evolution of those same particles in the 3D-d case, and the bottom two rows correspond to the 3D-h simulation. In the top panels for each case (horizontal), in the background in grayscale is the backward-time FTLE. In the vertical, the trajectory for every 10th particle is shown in gray.

At short times (<15 days), the trajectories from daily velocities show minor filamentation near the vortex edges, but most of the particles stay close to the eddy core. However, at longer times (30 and 60 days), a large number of the particles are scattered horizontally quite far from the eddy core. The scattering of particles is enhanced for the hourly velocity fields. Interestingly, while we see strong filamentary motion with daily velocities, the filaments themselves appear blurry in the hourly cases. This might be the influence of tides and IGWs, or it could be spurious, due to aliasing of even higher motions in the hourly velocity snapshots.

Vertical motion is also strongly dependent on filtering. For all the eddies, the particles are contained within the eddy boundary for the 3D-w case, with no or minimal vertical migration. While at short times (<15 days), the 3D particles stay pretty close to the surface for daily averaged velocities, they exhibit significant vertical motion at long times (>50 days). Vertical motion is the strongest for hourly velocities and the particles are subducted deeper than 200 m in certain regions.

After examining a large number of structures, we noticed two main categories of RCLV: expanding, and contracting. Such patterns were also observed by *Tarshish et al.* [2018], and the dynamics driving this motion are the subject of an ongoing study. We show particle trajectories from example RCLVs drawn from each of these three categories in Fig. 15 for the 3D-w case. The first kind (RCLV 1, which is the same as the red RCLV in Fig. 14) is an expanding eddy. We notice that, for the 3Dw case, the area covered by the eddy at the start of particle advection (represented by the cyan dots) is smaller than the area covered by the eddy at 60 days (magenta dots). This is due to a divergence inside the eddy, presumably associated with upwelling inside the eddy core. However, such upwelling cannot be observed directly in our particle advection experiments, since all the the particles were initialized at the surface, but is more clearly demonstrated in the salinity field. The second RCLV (right panel, RCLV 2) is a case of a shrinking eddy. Shrinking is likely due to convergence inside the eddy, which can be observed from the pronounced downwelling of the particles at 60 days, even for the weekly velocities. In Figs. 16 - 17, the positions of the same particles (cyan dots in Fig. 15), advected offline by the 3D hourly velocities, are plotted alongside the salinity field (calculated online in the llc4320 simulation) at initial and final times (60 days) .

This scattering of particles away from the eddy core, observed in Fig. 14 by unfiltered velocities, is most pronounced for the expanding eddy (RCLV 1; Fig. 16) and least pronounced for the contracting eddy (RCLV 2; Fig. 17), for which the large-scale divergence counteracts the dispersion.

Fig. 17 shows that the downwelling of particles in the shrinking eddy case is associated with increasing salinity anomaly inside the core of the eddy (bottom panels), whereas the expanding eddy corresponding to RCLV 1 in Fig. 15 is associated with decreasing salinity anomaly inside the eddy core at depth (bottom right panel Fig. 16), likely indicative of net upwelling.

In all these cases, while the eddies do leak particles, the overall eddy signature is still visible as a central cluster of particles. This indicates that, while the overall shape and structure of the eddy inferred from the weekly averaged velocities is persistent, there exist no clear material contour to define the eddy boundary that can be identified by the LAVD technique. Thus, from a Lagrangian point of view, the eddies inferred to be closed and coherent from weekly-averaged velocities are generally leaky for velocities with resolved submesoscales and IGWs/tides.

5.4 Vertical Motion

To get a comprehensive view of the vertical motion with the filtered and unfiltered velocities, we examine the depths reached by the 3D particles at different times. Fig. 18 shows a map of particle

depths at the end of 30 days for the three velocities for example. The hourly velocity fields transport particles vertically to depths of few 100m, with the strongest migration being qualitatively collocated with regions of strongest vorticity. This vertical excursion of particles is greatly reduced by temporal filtering, as a consequence of which, for the lowest temporal resolution (*i.e* for the weekly filter) the particles are surface restricted for the most part. In addition, the distribution of the particle depth at different times (Fig. 19) throws some light on the time dependence of vertical migration of particles. For hourly velocities, the particles migrate to a few hundred meters very quickly, and the median depth stays around 120 m for all times, with the number of particles reaching such depths increasing with time. For the daily velocities, a lot of the particles stay near the surface in the beginning (up to 40 days) with enhanced downelling at later times. The fact that there is reduced vertical motion with the low pass filtering indicates that there is a strong signature of vertical upwelling/downwelling due to submesoscale/IGWs inside the mesoscale eddies that is lost by temporal filtering. This is also in line with our earlier observation that the temporal filter makes the flow more rotational, filtering out the submesoscale/IGWs, and therefore results in a more 2D flow.

6 Discussion and Conclusions

In this study, we studied the Lagrangian transport properties associated with model velocities from a very high resolution (1/48° horizontal) numerical model (MITgcm) simulation (llc4320) in a part of the South Atlantic Ocean, covering the Agulhas retroflection and part of the ACC. Our primary aim was to identify the influence of fast-timescale motions on Lagrangian transport in this new type of ocean model.

The power spectral density in frequency space of the surface KE from the hourly model output velocity fields revealed the presence of strong IGWs and tides in the domain. We time averaged this hourly output over daily and weekly timescales to generate two additional velocity records. The wavenumber power spectrum corresponding to the three velocity fields (hourly unfiltered, daily filtered and weekly filtered) showed that time averaging predominantly acts to remove energy from smaller length scales. A Helmholtz decomposition of the 1D wavenumber spectrum [*Bühler et al.*, 2014; *Rocha et al.*, 2016a] into horizontally non-divergent and divergent components revealed that temporal filtering removes unbalanced divergent motions more effectively than the balanced geostrophic motions. Although we did not explictly perform an observing system simulation experiment, we noted that, among our different experiments, the weekly filtered velocities represent the closest approximation to velocities inferred from satellite altimetry.

We then used the three sets of velocity fields to advect particles at the surface using only the horizontal components of the velocity field (2D particles), and in full depth using all three components of the velocity field (3D particles). Using these Lagrangian trajectories, we computed some bulk transport statistics, relative dispersion and diffusivity, and also measures of kinematic coherence, FTLE and LAVD.

Relative dispersion and relative diffusivity calculations showed that the high frequency motions play a significant role in lateral transport, particularly at small scales. Temporal filtering reduced the effectiveness of turbulent diffusion at smaller scales and faster times, with the reduction in diffusion being greater for the weekly filter than the daily filter. The diffusivity at the largest scales was also reduced, but this impact was smaller than the reduction at the smaller scale. For the Agulhas region, the difference between the diffusivities from unfiltered and filtered velocities at small scales was greater than that for the ACC region. This might be caused by the ACC having a less energetic submesoscale velocity field than the Agulhas region, which can also be seen in the KE spectrum. A weaker submesoscale field might be a result of the model resolution being inadequate in the ACC, where the deformation radius is smaller, or because of the mean flow suppressing the growth of submesoscale instabilities [*Taylor et al.*, 2018].

Our coherent structure diagnostics generally showed that Lagrangian coherence was degraded when using the unfiltered and daily velocities, compared to the weekly averaged velocities. FTLE fields appeared noisy for hourly velocities at long times, and we did not observe the characteristic large scale, well defined FTLE ridges that are typically seen in studies with altimetry derived velocities [*Beron-Vera et al.*, 2008] even with daily averaged velocities, as the large scale transport barriers got drowned in the intricate submesoscale structures. Weekly averaged velocity fields produced more coherent material transport barriers in the FTLE field.

Using the LAVD method of *Haller et al.* [2016], we identified RCLVs over a range of convexity deficiency parameters for the raw and filtered velocities. We found that large-scale coherent RCLVs are only readily identifiable in weekly averaged velocities. While we found RCLVs with daily filtered velocities, they were very small and short lived. With hourly velocites, we only found RCLVs with unreasonably large convexity deficiency values. We examined the trajectories in the vicinity of the RCLVs identified from the weekly data to further understand how high-frequency flows caused material coherence to break down. At daily resolution, strong filaments appeared around the boundaries of the eddies. At hourly resolution, these filaments blurred into broader patches.

Perhaps the most important and controversial finding of our study relate to the nature of coherent mesoscale eddies (Agulhas rings specifically). A major question for mesoscale oceanography is *what fraction of the overall turbulent transport of tracers arises from trapping and translation of fluid within coherent eddies*. Some studies using Eulerian eddy tracking methods [e.g. *Dong et al.*, 2014] have estimated this fraction to be quite high. Recently, objective Lagrangian methods, driven by AVISO-derived velocities, have been applied to this question in different regions of the ocean [*Wang et al.*, 2016; *Abernathey and Haller*, 2017], largely concluding that Eulerian eddy tracking approaches overestimate the coherent transport. However, despite the precision and objectivity of the Lagrangian approach, these estimates are only as reliable as the velocities use to generate the trajectories. Do submesoscale flows, tides, and IGWs substantially alter mesoscale Lagrangian coherent structures?

To date, the most comprehensive studies of this question can be found in a recent pair of papers focused on a single eddy in the Gulf of Mexico. *Olascoaga et al.* [2017] identified this eddy using the objective geodesic method [*Haller and Beron-Vera*, 2013; *Wang et al.*, 2015] applied to AVISO-derived velocities. They argued that evidence from other observations, particularly drogued surface drifters and remotely sensed ocean color, confirmed the coherent, material nature of the identified eddy boundary and was consistent with the $\sim$ 200 day lifetime. However, the same geodesic method applied to velocities from a submesoscale permitting, data-assimilating simulation at 1 km resolution failed to identify any coherent structure, despite the fact that relative dispersion statistics from the simulated trajectories agreed well with drifter statistics. The authors speculated that this failure could be an artifact of the data assimilation process, related to more general challenges of ocean data assimilation in the submesoscale regime [*Sandery and Sakov*, 2017]. Studying the same eddy, however, [*Beron-Vera et al.*, 2018] reached a slightly different conclusion: while the geodesic eddy method was too strict to find any Lagrangian coherent structure, the LAVD method was more successful. With a high enough choice of convexity deficiency, mesoscale eddies were shown to persist, even though their boundaries exhibited increased filamentation relative to the extremely coherent boundaries inferred from satellite altimetry. Taken together, these studies give a mixed assessment of the role of the submesoscale: is the difficulty of finding coherent mesoscale eddies in submesoscale-permitting simulations a problem with the model, or with the method? More broadly, how general are the conclusions that can be drawn from the study of single eddy?

Our experiments avoid the confounding effects of data assimilation and examine a much broader spatial area. The submesoscale [*Rocha et al.*, 2016a,b] and IGW / tidal variability [*Savage et al.*, 2017] in the LLC simulation agrees reasonably well with in-situ observations in the wavenumber and frequency domain, showing that the amplitude of these motions is physically plausible. We find

that the Agulhas rings detected from weekly averaged velocities are much more coherent than the "true" Agulhas rings, as represented by the daily or hourly velocities. The high-frequency motions cause material to leak substantially across the eddy boundaries identified from the weekly averaged flow. While visual examination of the trajectories shows there appears to be a Lagrangian core to the eddies, material boundaries are not readily identifiable using the LAVD approach. Most LCS identification methods have been validated using two-dimensional turbulence as a test case [*Hadjighasem et al.*, 2017], which is arguably dynamically similar to the weekly averaged flow. Our study thus suggests that new approaches to identifying materially coherent eddies may be needed in the regime represented by the LLC simulation.

We attribute this breakdown of observed coherence at high temporal resolutions to the submesoscale and IGW/tidal signature in high frequency data. The absence of small scale motions associated with the IGW and submesoscale currents, in low temporal resolution data, may lead to overestimating Lagrangian coherence in satellite altimetry derived fields. As such we should exercise caution and account for these biases when make transport estimates from high-spatial-resolution but temporally sparse satellite altimetry derived geostrophic veocities. The present results therefore have implications for high resolution altimeters, for example, the upcoming Surface Water and Ocean Topography (SWOT) mission. As in current altimeter technology, swath altimetry (SWOT) will likely alias high-frequency motions. Further, unbalanced flows may upset the estimation of O(10 km) resolution surface geostrophic velocities. That is, the high-wavenumber sea surface height variability may represent a different, ageostrophic, physical regime, where geostrophy might not be the best route to infer velocities. Tidal and supertidal motions, aliased by satellite altimetry, will need to be properly understood if we are to gain meaningful insight regarding the dynamics of both high and low-frequency motions at small scales from this upcoming mission. These are some of the problems that merit further investigation.

References

Abernathey, R., and D. Ferreira (2015), Southern ocean isopycnal mixing and ventilation changes driven by winds, *Geophysical Research Letters*, *42*(23), 10,357–10,365, doi:10.1002/2015GL066238.

Abernathey, R., and G. Haller (2017), Transport by Lagrangian Vortices in the Eastern Pacific, *ArXiv e-prints*.

Abernathey, R. P., and J. Marshall (2013), Global surface eddy diffusivities derived from satellite altimetry, *Journal of Geophysical Research: Oceans*, *118*(2), 901–916.

Abraham, E. R., and M. M. Bowen (2002), Chaotic stirring by a mesoscale surface-ocean flow, *Chaos: An Interdisciplinary Journal of Nonlinear Science*, *12*(2), 373–381.

Alford, M. H., J. A. MacKinnon, H. L. Simmons, and J. D. Nash (2016), Near-inertial internal gravity waves in the ocean, *Annual review of marine science*, *8*, 95–123.

Aluie, H., M. Hecht, and G. K. Vallis (2018), Mapping the energy cascade in the north atlantic ocean: The coarse-graining approach, *Journal of Physical Oceanography*, *48*(2), 225–244, doi:10.1175/JPO-D-17-0100.1.

Babiano, A., C. Basdevant, P. Le Roy, and R. Sadourny (1990), Relative dispersion in two-dimensional turbulence, *Journal of Fluid Mechanics*, *214*, 535–557.

Balwada, D., J. H. LaCasce, and K. G. Speer (2016), Scale-dependent distribution of kinetic energy from surface drifters in the gulf of mexico, *Geophysical Research Letters*, *43*(20), 10,856–10,863, doi:10.1002/2016GL069405, 2016GL069405.

Balwada, D., K. S. Smith, and R. Abernathey (2018), Role of (sub)mesoscale generated vertical velocities in tracer subduction, *Geophysical Research Letters*.

Barkan, R., K. B. Winters, and J. C. McWilliams (2017), Stimulated imbalance and the enhancement of eddy kinetic energy dissipation by internal waves, *Journal of Physical Oceanography*, *47*(1), 181–198, doi:10.1175/JPO-D-16-0117.1.

Bennett, A. F. (1984), Relative dispersion: Local and nonlocal dynamics, *Journal of the Atmospheric Sciences*, *41*(11), 1881–1886, doi:10.1175/1520-0469(1984)041<1881:RDLAND>2.0.CO;2.

Beron-Vera, F., M. Olascoaga, and G. Goni (2008), Oceanic mesoscale eddies as revealed by lagrangian coherent structures, *Geophysical Research Letters*, *35*(12).

Beron-Vera, F., A. Hadjighasem, O. Xia, M. Olascoaga, and G. Haller (2018), Coherent lagrangian swirls among submesoscale motions, *Proceedings of the National Academy of Sciences*, doi:10.1073/pnas.1701392115.

Beron-Vera, F. J. (2010), Mixing by low- and high-resolution surface geostrophic currents, *Journal of Geophysical Research: Oceans*, *115*(C10), doi:10.1029/2009JC006006.

Beron-Vera, F. J., Y. Wang, M. J. Olascoaga, G. J. Goni, and G. Haller (2013), Objective detection of oceanic eddies and the agulhas leakage, *Journal of Physical Oceanography*, *43*(7), 1426–1438.

Bühler, O., J. Callies, and R. Ferrari (2014), Wave–vortex decomposition of one-dimensional ship-track data, *Journal of Fluid Mechanics*, *756*, 1007–1026.

Callies, J., R. Ferrari, and O. Bühler (2014), Transition from geostrophic turbulence to inertia–gravity waves in the atmospheric energy spectrum, *Proceedings of the National Academy of Sciences*, *111*(48), 17,033–17,038, doi:10.1073/pnas.1410772111.

Capet, X., J. C. McWilliams, M. J. Molemaker, and A. F. Shchepetkin (2008), Mesoscale to submesoscale transition in the california current system. part i: Flow structure, eddy flux, and observational tests, *Journal of Physical Oceanography*, *38*(1), 29–43, doi:10.1175/2007JPO3671.1.

Chelton, D. B., M. G. Schlax, R. M. Samelson, and R. A. de Szoeke (2007), Global observations of large oceanic eddies, *Geophysical Research Letters*, *34*(15), doi:10.1029/2007GL030812.

Choi, J., A. Bracco, R. Barkan, A. F. Shchepetkin, J. C. McWilliams, and J. M. Molemaker (2017), Submesoscale dynamics in the northern gulf of mexico. part iii: Lagrangian implications, *Journal of Physical Oceanography*, *47*(9), 2361–2376, doi:10.1175/JPO-D-17-0036.1.

D'Asaro, E., C. Lee, L. Rainville, R. Harcourt, and L. Thomas (2011), Enhanced turbulence and energy dissipation at ocean fronts, *Science*, *332*(6027), 318–322, doi:10.1126/science.1201515.

Dong, C., J. C. McWilliams, Y. Liu, and D. Chen (2014), Global heat and salt transports by eddy movement, *Nature Communications*, *5*, 3294 EP –.

d'Ovidio, F., J. Isern-Fontanet, C. Lopez, E. Hernandez-Garcia, and E. Garcia-Ladona (2009), Comparison between eulerian diagnostics and finite-size lyapunov exponents computed from altimetry in the algerian basin, *Deep Sea Research Part I: Oceanographic Research Papers*, *56*(1), 15 – 31, doi:https://doi.org/10.1016/j.dsr.2008.07.014.

Ducet, N., P. Y. Le Traon, and G. Reverdin (2000), Global high-resolution mapping of ocean circulation from topex/poseidon and ers-1 and -2, *Journal of Geophysical Research: Oceans*, *105*(C8), 19,477–19,498, doi:10.1029/2000JC900063.

Elipot, S., R. Lumpkin, R. C. Perez, J. M. Lilly, J. J. Early, and A. M. Sykulski (2016), A global surface drifter data set at hourly resolution, *Journal of Geophysical Research: Oceans*, *121*(5), 2937–2966.

Farazmand, M., and G. Haller (2012), Computing lagrangian coherent structures from their variational theory, *Chaos: An Interdisciplinary Journal of Nonlinear Science*, *22*(1), 013,128.

Ferrari, R., and C. Wunsch (2009), Ocean circulation kinetic energy: Reservoirs, sources, and sinks, *Annual Review of Fluid Mechanics*, *41*.

Fjortoft, R., J.-M. Gaudin, N. Pourthié, J.-C. Lalaurie, A. Mallet, J.-F. Nouvel, J. Martinot-Lagarde, H. Oriot, P. Borderies, C. Ruiz, and S. Daniel (2014), Karin on swot: Characteristics of near-nadir ka-band interferometric sar imagery, *IEEE Transactions on Geoscience and Remote Sensing*, *52*, 2172–2185.

Foussard, A., S. Berti, X. Perrot, and G. Lapeyre (2017), Relative dispersion in generalized two-dimensional turbulence, *Journal of Fluid Mechanics*, *821*, 358–383.

Fox-Kemper, B., R. Ferrari, and R. Hallberg (2008), Parameterization of mixed layer eddies. part i: Theory and diagnosis, *Journal of Physical Oceanography*, *38*(6), 1145–1165, doi:10.1175/2007JPO3792.1.

Fu, L. L., and R. Ferrari (2008), Observing mesoscale to submesoscale dynamics today, and in the future with SWOT, *EOS*, *89*, 2689âĂŞ2691, doi:10.1109/IGARSS.2011.6049757.

Gent, P. R., and J. C. Mcwilliams (1990), Isopycnal mixing in ocean circulation models, *Journal of Physical Oceanography*, *20*(1), 150–155, doi:10.1175/1520-0485(1990)020<0150:IMIOCM>2.0.CO;2.

Gent, P. R., J. Willebrand, T. J. McDougall, and J. C. McWilliams (1995), Parameterizing eddy-induced tracer transports in ocean circulation models, *Journal of Physical Oceanography*, *25*(4), 463–474, doi:10.1175/1520-0485(1995)025<0463:PEITTI>2.0.CO;2.

Gnanadesikan, A., A. Russell, M.-A. Pradal, and R. Abernathey (2017), Impact of lateral mixing in the ocean on el nino in a suite of fully coupled climate models, *Journal of Advances in Modeling Earth Systems*, *9*(7), 2493–2513, doi:10.1002/2017MS000917.

Groeskamp, S., B. M. Sloyan, J. D. Zika, and T. J. McDougall (2017), Mixing inferred from an ocean climatology and surface fluxes, *Journal of Physical Oceanography*, *47*(3), 667–687, doi:10.1175/JPO-D-16-0125.1.

Groeskamp, S., R. P. Abernathey, and A. Klocker (2018), Water mass transformation by cabbeling and thermobaricity, *Geophysical Research Letters*, *43*(20), 10,835–10,845, doi:10.1002/2016GL070860.

Grooms, I., and L. Zanna (2017), A note on ÃćÂĂÂŸtoward a stochastic parameterization of ocean mesoscale eddiesÃćÂĂÂŹ, *Ocean Modelling*, *113*, 30 – 33, doi:https://doi.org/10.1016/j.ocemod.2017.03.007.

Hadjighasem, A., M. Farazmand, D. Blazevski, G. Froyland, and G. Haller (2017), A critical comparison of lagrangian methods for coherent structure detection, *Chaos: An Interdisciplinary*

Journal of Nonlinear Science, 27(5), 053,104.

Haller, G. (2002), Lagrangian coherent structures from approximate velocity data, *Physics of fluids*, *14*(6), 1851–1861.

Haller, G. (2011), A variational theory of hyperbolic lagrangian coherent structures, *Physica D: Nonlinear Phenomena*, *240*(7), 574–598.

Haller, G. (2015), Lagrangian coherent structures, *Annual Review of Fluid Mechanics*, *47*, 137–162.

Haller, G., and F. Beron-Vera (2013), Coherent lagrangian vortices: The black holes of turbulence, *Journal of Fluid Mechanics*, *731*.

Haller, G., and T. Sapsis (2011), Lagrangian coherent structures and the smallest finite-time lyapunov exponent, *Chaos: An Interdisciplinary Journal of Nonlinear Science*, *21*(2), 023,115.

Haller, G., and G. Yuan (2000), Lagrangian coherent structures and mixing in two-dimensional turbulence, *Physica D: Nonlinear Phenomena*, *147*(3), 352–370.

Haller, G., A. Hadjighasem, M. Farazmand, and F. Huhn (2016), Defining coherent vortices objectively from the vorticity, *Journal of Fluid Mechanics*, *795*, 136–173.

Isern-Fontanet, J., E. Garcia-Ladona, and J. Font (2006), Vortices of the mediterranean sea: An altimetric perspective, *Journal of Physical Oceanography*, *36*(1), 87–103, doi:10.1175/JPO2826.1.

Keating, S. R., K. S. Smith, and P. R. Kramer (2011), Diagnosing lateral mixing in the upper ocean with virtual tracers: Spatial and temporal resolution dependence, *Journal of Physical Oceanography*, *41*(8), 1512–1534.

Klein, P., and G. Lapeyre (2009), The oceanic vertical pump induced by mesoscale and submesoscale turbulence, *Annual review of marine science*, *1*, 351–375.

Klein, P., B. L. Hua, G. Lapeyre, X. Capet, S. Le Gentil, and H. Sasaki (2008), Upper ocean turbulence from high-resolution 3d simulations, *Journal of Physical Oceanography*, *38*(8), 1748–1763.

Klocker, A., and R. Abernathey (2014), Global patterns of mesoscale eddy properties and diffusivities, *Journal of Physical Oceanography*, *44*(3), 1030–1046, doi:10.1175/JPO-D-13-0159.1.

LaCasce, J. (2008), Statistics from lagrangian observations, *Progress in Oceanography*, *77*(1), 1–29.

Large, W. G., and S. Yeager (2004), Diurnal to decadal global forcing for ocean and sea-ice models: The data sets and flux climatologies, *Tech. rep.*, NCAR/UCAR, doi:http://dx.doi.org/10.5065/D6KK98Q6.

Le Traon, P. Y., P. Klein, B. L. Hua, and G. Dibarboure (2008), Do altimeter wavenumber spectra agree with the interior or surface quasigeostrophic theory?, *Journal of Physical Oceanography*, *38*(5), 1137–1142, doi:10.1175/2007JPO3806.1.

Lumpkin, R., and G. C. Johnson (2013), Global ocean surface velocities from drifters: Mean, variance, el niÃČÂśoÃćÂĂÂŞsouthern oscillation response, and seasonal cycle, *Journal of Geophysical Research: Oceans*, *118*(6), 2992–3006, doi:10.1002/jgrc.20210.

Mahadevan, A. (2016), The impact of submesoscale physics on primary productivity of plankton, *Annual Review of Marine Science*, *8*(1), 161–184, doi:10.1146/annurev-marine-010814-015912, pMID: 26394203.

Mahadevan, A., and J. W. Campbell (2002), Biogeochemical patchiness at the sea surface, *Geophysical Research Letters*, *29*(19), 32–1–32–4, doi:10.1029/2001GL014116.

Mariano, A., V. Kourafalou, A. Srinivasan, H. Kang, G. Halliwell, E. Ryan, and M. Roffer (2011), On the modeling of the 2010 gulf of mexico oil spill, *Dynamics of Atmospheres and Oceans*, *52*(1-2), 322–340.

Marshall, J., J. R. Scott, A. Romanou, M. Kelley, and A. Leboissetier (2017), The dependence of the oceanÃćÂĂÂŹs moc on mesoscale eddy diffusivities: A model study, *Ocean Modelling*, *111*, 1 − 8, doi:https://doi.org/10.1016/j.ocemod.2017.01.001.

Martin, A. (2003), Phytoplankton patchiness: The role of lateral stirring and mixing, *57*, 125–174.

Maxey, M. R., and J. J. Riley (1983), Equation of motion for a small rigid sphere in a nonuniform flow, *The Physics of Fluids*, *26*(4), 883–889, doi:10.1063/1.864230.

McWilliams, J. C. (2016), Submesoscale currents in the ocean, in *Proc. R. Soc. A*, vol. 472, p. 20160117, The Royal Society.

Munk, W. (1981), Internal waves and small-scale processes., in *Evolution of Physical Oceanography: Scientific Surveys in Honor of Henry Stommel*, edited by B. A. Warren and C. Wunsch, 9, pp. 264 − 291, MIT Press.

Okubo, A. (1971), Oceanic diffusion diagrams, *Deep Sea Research and Oceanographic Abstracts*, *18*(8), 789 − 802, doi:https://doi.org/10.1016/0011-7471(71)90046-5.

Olascoaga, M., F. Beron-Vera, Y. Wang, J. Triñanes, and P. Pérez-Brunius (2017), On the significance of coherent lagrangian eddies detected from satellite altimetry, *arXiv preprint arXiv:1704.06186*.

Omand, M. M., E. A. DâĂŹAsaro, C. M. Lee, M. J. Perry, N. Briggs, I. Cetinić, and A. Mahadevan (2015), Eddy-driven subduction exports particulate organic carbon from the spring bloom, *Science*, *348*(6231), 222–225.

Pierrehumbert, R. T., and H. Yang (1993), Global chaotic mixing on isentropic surfaces, *Journal of the Atmospheric Sciences*, *50*(15), 2462–2480, doi:10.1175/1520-0469(1993)050<2462:GCMOIS> 2.0.CO;2.

Poje, A. C., T. M. Özgökmen, B. L. Lipphardt, B. K. Haus, E. H. Ryan, A. C. Haza, G. A. Jacobs, A. Reniers, M. J. Olascoaga, G. Novelli, et al. (2014), Submesoscale dispersion in the vicinity of the deepwater horizon spill, *Proceedings of the National Academy of Sciences*, *111*(35), 12,693–12,698.

Qiu, B., S. Chen, P. Klein, C. Ubelmann, L.-L. Fu, and H. Sasaki (2016), Reconstructability of three-dimensional upper-ocean circulation from swot sea surface height measurements, *Journal of Physical Oceanography*, *46*(3), 947–963, doi:10.1175/JPO-D-15-0188.1.

Qiu, B., S. Chen, P. Klein, J. Wang, H. Torres, L.-L. Fu, and D. Menemenlis (2018), Seasonality in transition scale from balanced to unbalanced motions in the world ocean, *Journal of Physical Oceanography*, *48*(3), 591–605, doi:10.1175/JPO-D-17-0169.1.

Roach, C. J., D. Balwada, and K. Speer (2016), Horizontal mixing in the southern ocean from argo float trajectories, *Journal of Geophysical Research: Oceans*, *121*(8), 5570–5586, doi:10.1002/2015JC011440.

Roach, C. J., D. Balwada, and K. Speer (2018), Global observations of horizontal mixing from argo float and surface drifter trajectories, *Journal of Geophysical Research: Oceans*, *123*(7), 4560–4575, doi:10.1029/2018JC013750.

Rocha, C. B., T. K. Chereskin, S. T. Gille, and D. Menemenlis (2016a), Mesoscale to submesoscale wavenumber spectra in drake passage, *Journal of Physical Oceanography*, *46*(2), 601–620.

Rocha, C. B., S. T. Gille, T. K. Chereskin, and D. Menemenlis (2016b), Seasonality of submesoscale dynamics in the kuroshio extension, *Geophysical Research Letters*, *43*(21), 11,304–11,311, doi:10.1002/2016GL071349.

Rypina, I. I., I. Kamenkovich, P. Berloff, and L. J. Pratt (2012), Eddy-induced particle dispersion in the near-surface north atlantic, *Journal of Physical Oceanography*, *42*(12), 2206–2228.

Sandery, P. A., and P. Sakov (2017), Ocean forecasting of mesoscale features can deteriorate by increasing model resolution towards the submesoscale, *Nature Communications*, *8*(1), 1566, doi:10.1038/s41467-017-01595-0.

Savage, A. C., B. K. Arbic, M. H. Alford, J. K. Ansong, J. T. Farrar, D. Menemenlis, A. K. O'Rourke, J. G. Richman, J. F. Shriver, G. Voet, A. J. Wallcraft, and L. Zamudio (2017), Spectral decomposition of internal gravity wave sea surface height in global models, *Journal of Geophysical Research: Oceans*, *122*(10), 7803–7821, doi:10.1002/2017JC013009.

Shakespeare, C. J., and A. M. Hogg (2017), Spontaneous surface generation and interior amplification of internal waves in a regional-scale ocean model, *Journal of Physical Oceanography*, *47*(4), 811–826, doi:10.1175/JPO-D-16-0188.1.

Tarshish, N., R. Abernathey, C. Zhang, C. O. Dufourd, I. Frenger, and S. M. Griffies (2018), Identifying lagrangian coherent structures in a mesoscale eddy-permitting ocean model, *Ocean Modelling*.

Taylor, J. R., S. Bachman, M. Stamper, P. Hosegood, K. Adams, J.-B. Sallee, and R. Torres (2018), Submesoscale rossby waves on the antarctic circumpolar current, *Science Advances*, *4*(3), doi: 10.1126/sciadv.aao2824.

van der Walt, S., J. L. Schönberger, J. Nunez-Iglesias, F. Boulogne, J. D. Warner, N. Yager, E. Gouillart, and T. Yu (2014), scikit-image: Image processing in python, *PeerJ*, *2*, e453, doi: 10.7717/peerj.453.

Van Sebille, E., M. H. England, and G. Froyland (2012), Origin, dynamics and evolution of ocean garbage patches from observed surface drifters, *Environmental Research Letters*, *7*(4), 044,040.

Wagner, G. L., and W. R. Young (2016), A three-component model for the coupled evolution of near-inertial waves, quasi-geostrophic flow and the near-inertial second harmonic, *Journal of Fluid Mechanics*, *802*, 806âĂŞ837, doi:10.1017/jfm.2016.487.

Wang, J., L.-L. Fu, B. Qiu, D. Menemenlis, J. T. Farrar, Y. Chao, A. F. Thompson, and M. M. Flexas (2018), An observing system simulation experiment for the calibration and validation of the surface water ocean topography sea surface height measurement using in situ platforms, *Journal of Atmospheric and Oceanic Technology*, *35*(2), 281–297, doi:10.1175/JTECH-D-17-0076.1.

Wang, Y., M. J. Olascoaga, and F. J. Beron-Vera (2015), Coherent water transport across the south atlantic, *Geophysical Research Letters*, *42*(10), 4072–4079, doi:10.1002/2015GL064089, 2015GL064089.

Wang, Y., F. Beron-Vera, and M. Olascoaga (2016), The life cycle of a coherent lagrangian agulhas ring, *Journal of Geophysical Research: Oceans*, *121*(6), 3944–3954.

Waugh, D. W., and E. R. Abraham (2008), Stirring in the global surface ocean, *Geophysical Research Letters*, *35*(20).

Waugh, D. W., E. R. Abraham, and M. M. Bowen (2006), Spatial variations of stirring in the surface ocean: A case study of the tasman sea, *Journal of Physical Oceanography*, *36*(3), 526–542.

Waugh, D. W., S. R. Keating, and M.-L. Chen (2012), Diagnosing ocean stirring: Comparison of relative dispersion and finite-time lyapunov exponents, *Journal of Physical Oceanography*, *42*(7), 1173–1185.

White, M. (2018), Carl wunsch and the rise of modern oceanography.

Zhang, Z., W. Wang, and B. Qiu (2014), Oceanic mass transport by mesoscale eddies, *Science*, *345*(6194), 322–324, doi:10.1126/science.1252418.
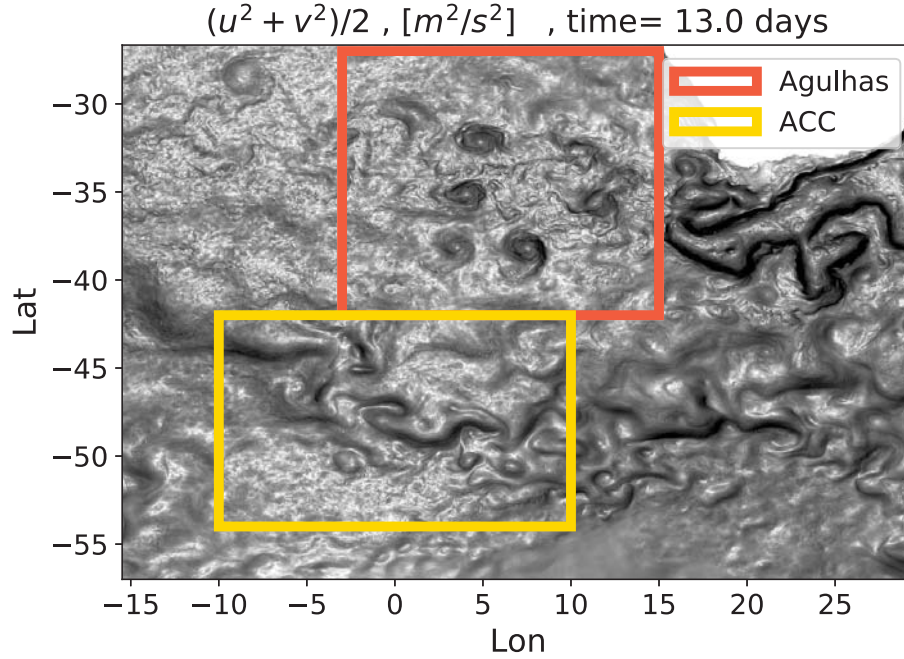
Figure 1: The domain with the specific sub-domains used for the relative diffusivity calculation. A snapshot of the surface KE in the domain, with the Agulhas / ACC regions marked in red / yellow. The relative diffusivity calculations (described in Section 4) were done in these two regions separately to study dispersion characteristics of flows dominated by coherent eddies (Agulhas) and strong zonal shear (ACC).

Zhurbas, V., and I. S. Oh (2004), Drifter-derived maps of lateral diffusivity in the pacific and atlantic oceans in relation to surface circulation patterns, *Journal of Geophysical Research: Oceans*, *109*(C5), doi:10.1029/2003JC002241.
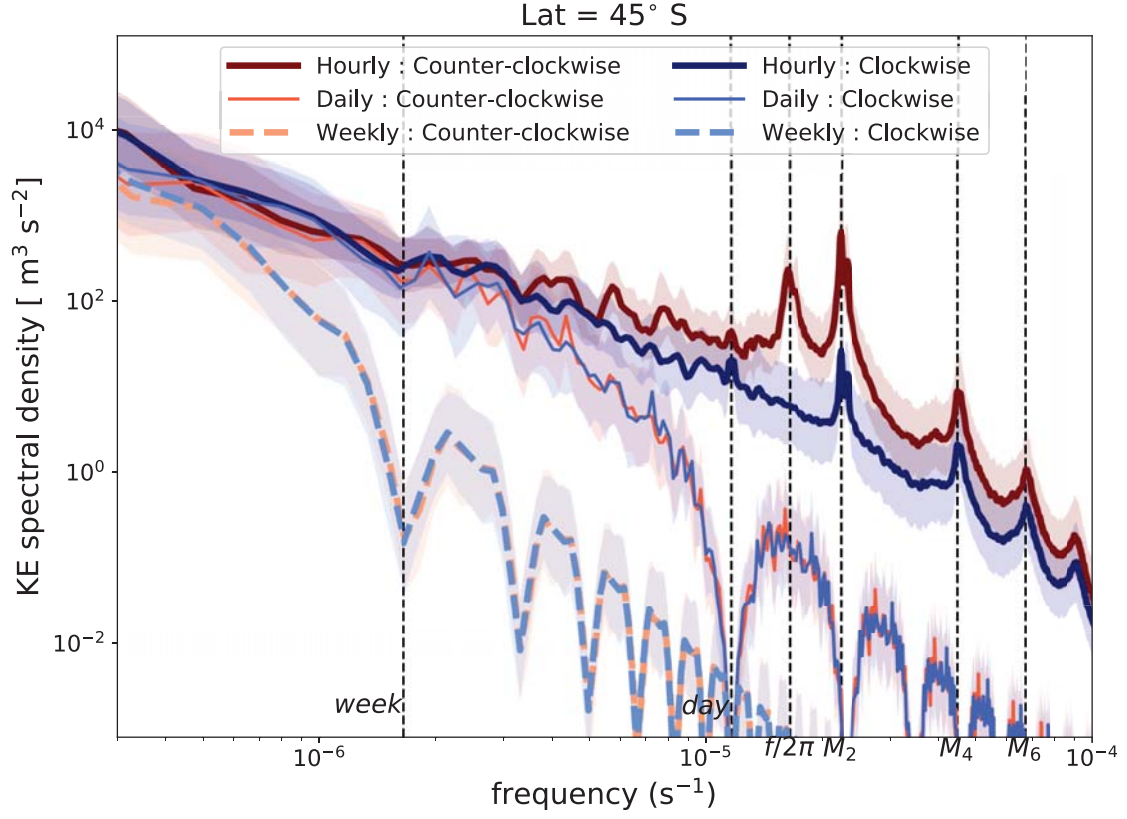
Figure 2: The frequency power spectral density (psd) of surface Kinetic Energy at $45°S$ for 73 days: The thick solid lines show the zonal mean (over $15.5°W$ - $29.5°E$) of psd from the hourly velocities output by the MITgcm llc4320. The thin lines corresponds to zonal mean of the psd calculated from the daily averaged velocities linearly interpolated to hourly intervals and the thick dashed lines correspond to the weekly averaged velocities also linearly interpolated to hourly intervals. The shading denotes the 1 standard deviation error (across the longitude bands). The spectra is split into a clockwise (blue) and a counter-clockwise (red) part by separating the positive and negative frequencies to isolate inertial oscillations.
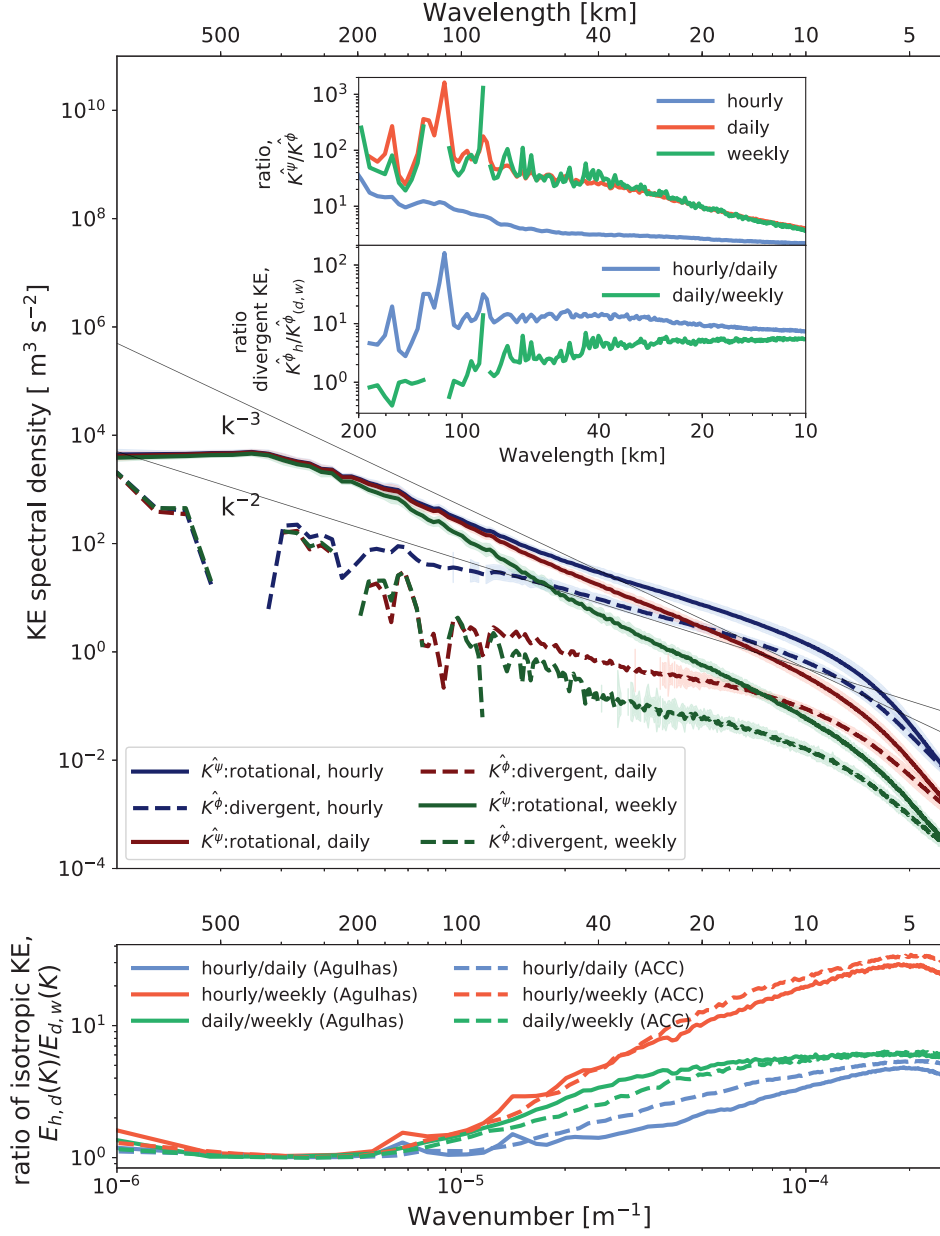
Figure 3: Top panel: Surface KE wavenumber spectra decomposed into the Rotational (solid) and Divergent (dashed) parts, [following *Bühler et al.*, 2014] for the hourly velocities, daily averaged velocities, and weekly averaged velocities from the llc4320 numerical model simulations. Top panel, upper inset: The ratios of the Rotational: Divergent components. Top panel, lower inset: The ratios of hourly:daily (blue) and daily:weekly (green) divergent KE . Bottom panel: The ratios of the unfiltered (hourly) and filtered (daily,weekly) isotropic surface KE, calculated separately for the Agulhas and ACC sectors shown in Fig. 1. The ratio of daily to weekly filtered velocities have also been shown for comparison.
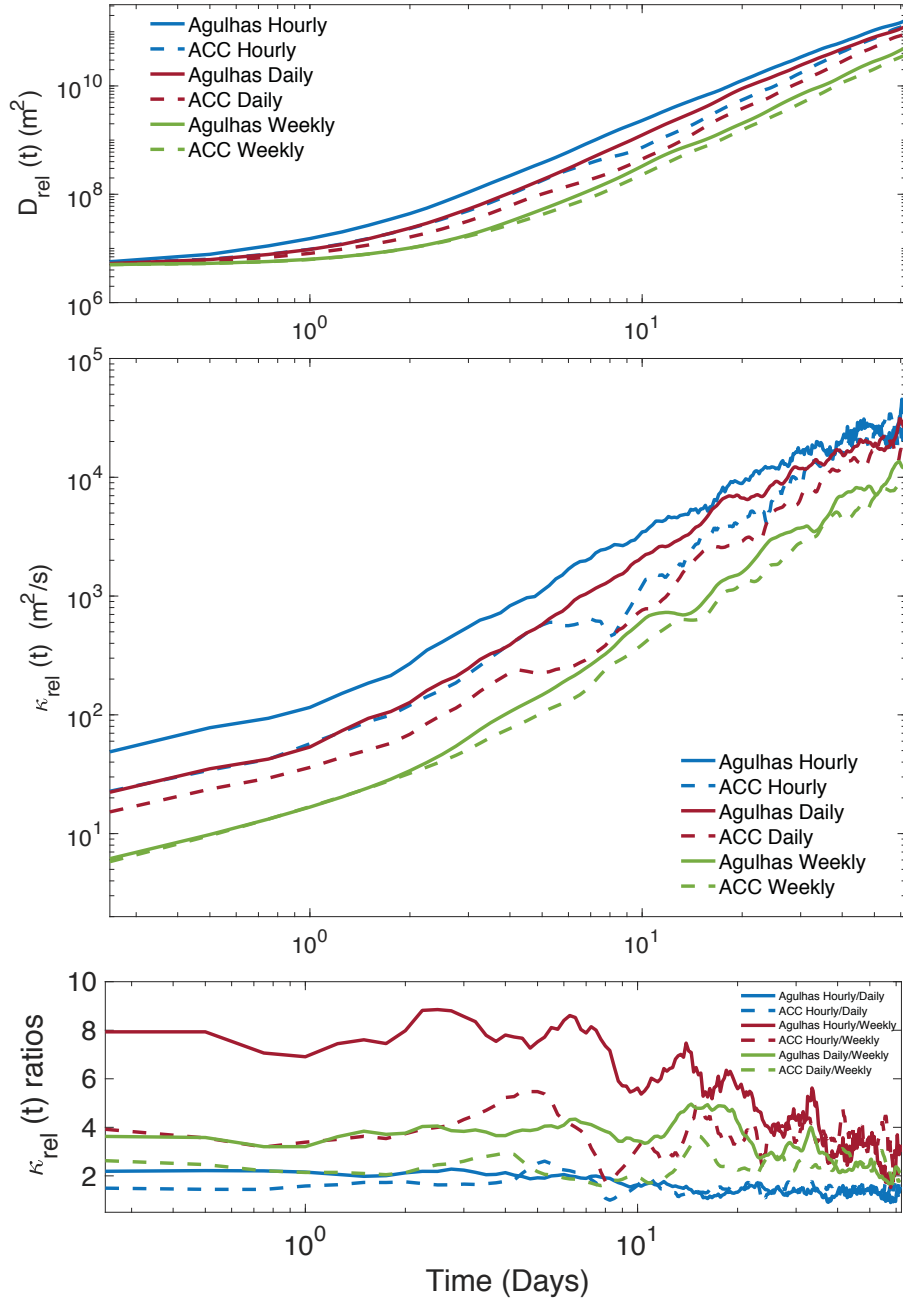
Figure 4: Surface relative dispersion (top), relative diffusivities (middle) and ratios of the relative diffusivities (bottom) as a function of time, in the Agulhas (solid) and the ACC (dashed), for the three 2D experiments.
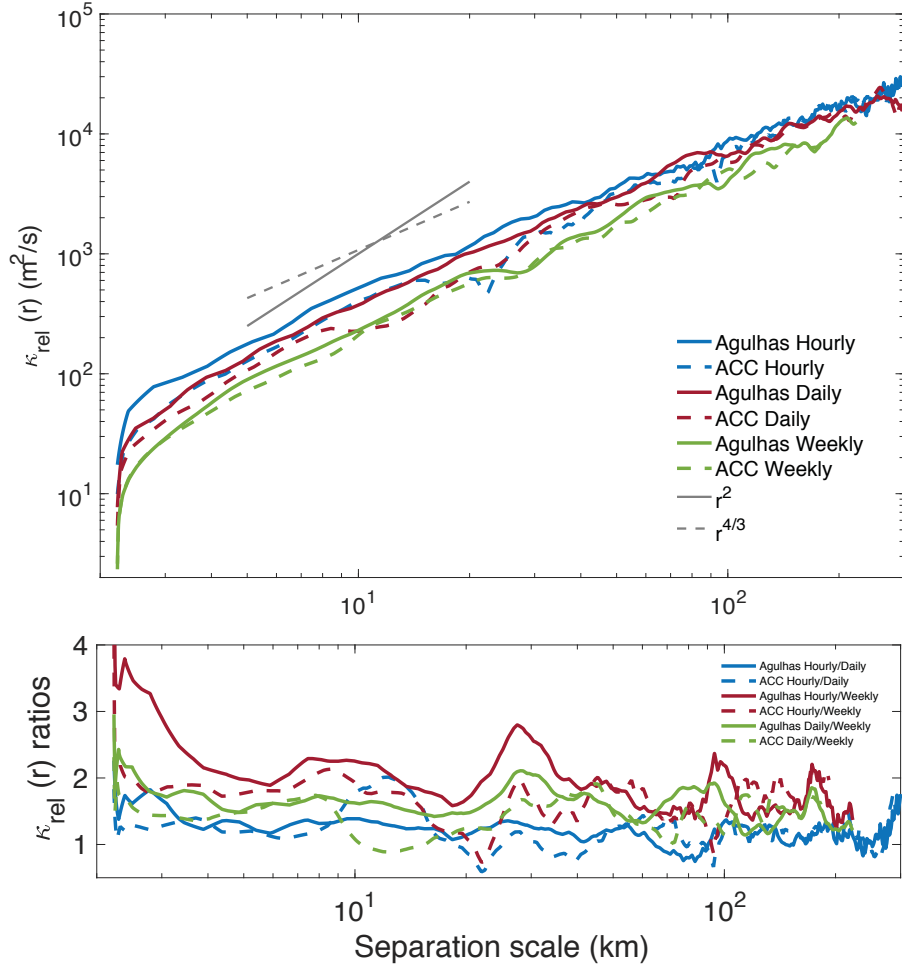
Figure 5: Surface relative diffusivities (top) and ratios of the diffusivities (bottom) in the Agulhas (solid), and the ACC (dashed), for the three 2D experiments as a function of the mean separation ($D_{rel}^{1/2}$).
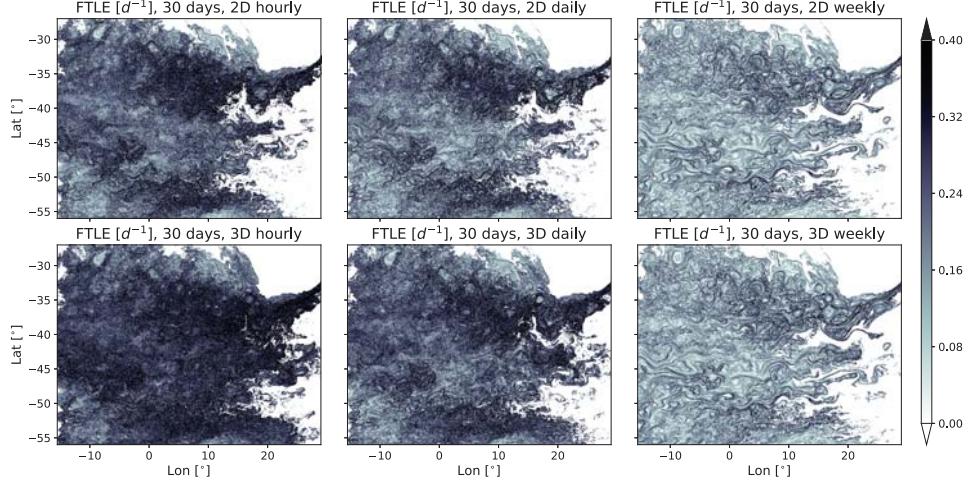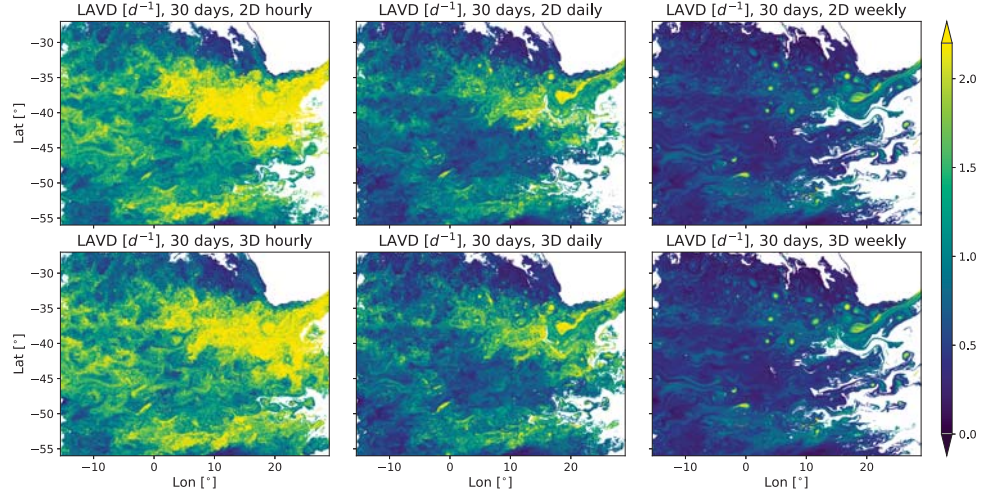
Figure 6: Finite time Lyapunov Exponents (FTLEs) after 30 days, for Lagrangian particles in the Agulhas sector advected by Hourly velocities (left), Daily averaged velocities (middle), and Weekly averaged velocities (right) from the llc4320 numerical model simulations. The top panels are for the 2D particles and bottom panels are for 3D particles. The mask (white) represents the initial positions of all particles that reached the edge of the domain at the end of the integration.
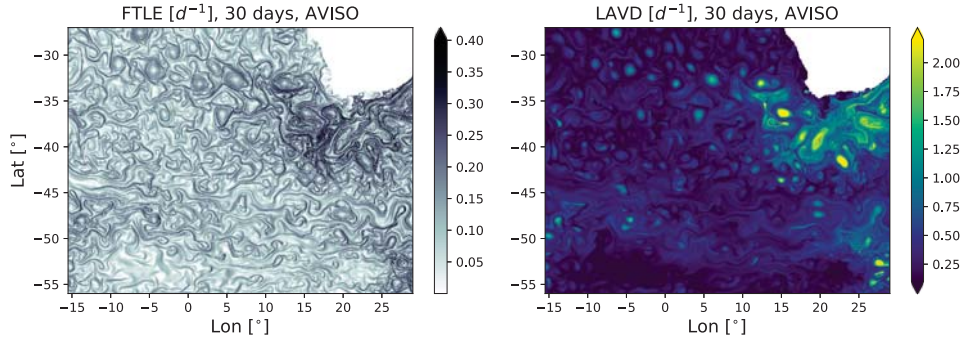

Figure 7: Finite time Lyapunov Exponents (FTLEs) (left panel) and Lagrangian averaged vorticity deviation (LAVD) (right panel) for particles advected by AVISO velocities after 30 days, shown for the Agulhas sector.
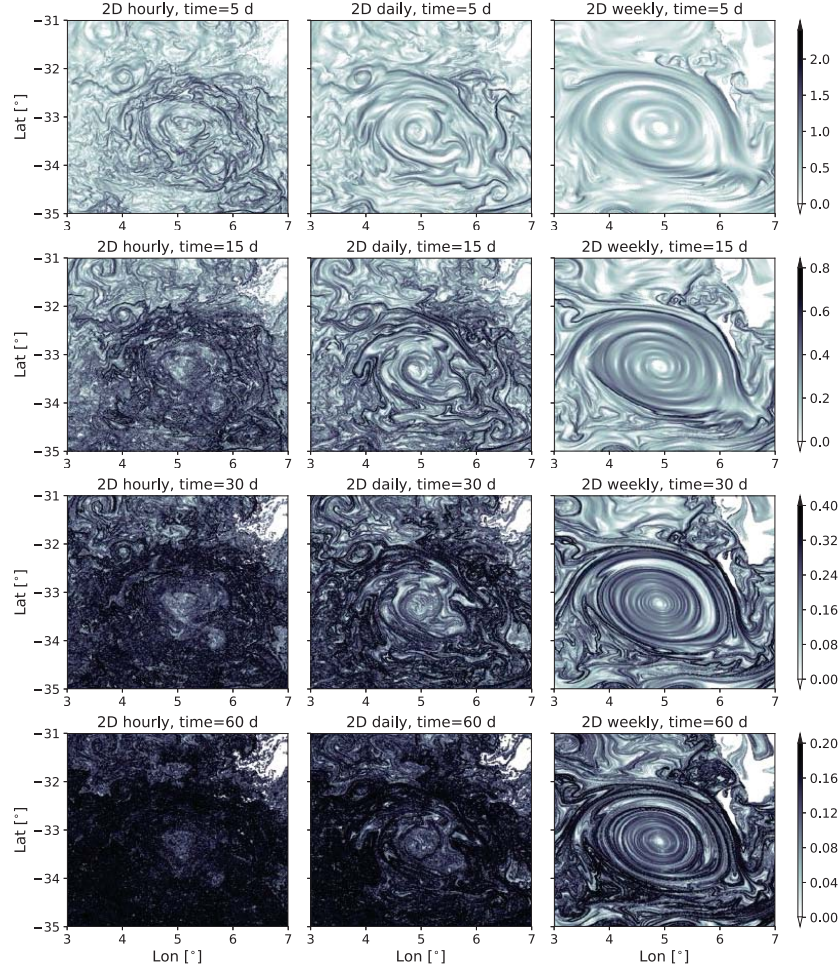
Figure 8: Snapshots of the FTLE field, zoomed in, near an eddy at different times, for the three 2D particle advection experiments with filtered and unfiltered llc4320 velocities.
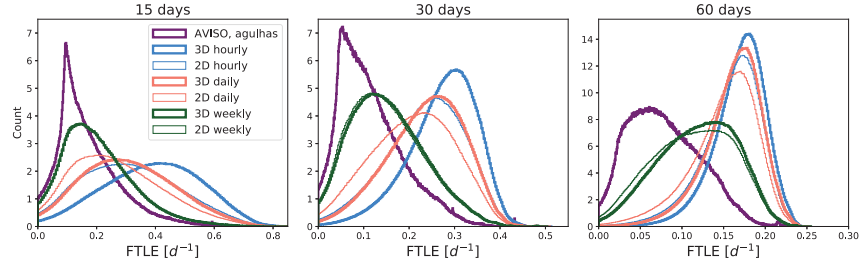
Figure 9: The distribution of the FTLE probability density function for the 6 particle advection experiments with filtered and unfiltered llc4320 velocities along with the FTLE distriution for the particle tracking experiment with AVISO velocity fields in the Agulhas sector.

Figure 10: LAVD integrated after 30 days, for Lagrangian particles in the Agulhas sector advected by Hourly velocities (left), Daily averaged velocities (middle), and Weekly averaged velocities (right) from the llc4320 numerical model simulations. The panels on the top are for the 2D particles and the panels on the bottom are for 3D particles. The mask (white) represents the initial positions of all particles that reached the edge of the domain at the end of the integration.
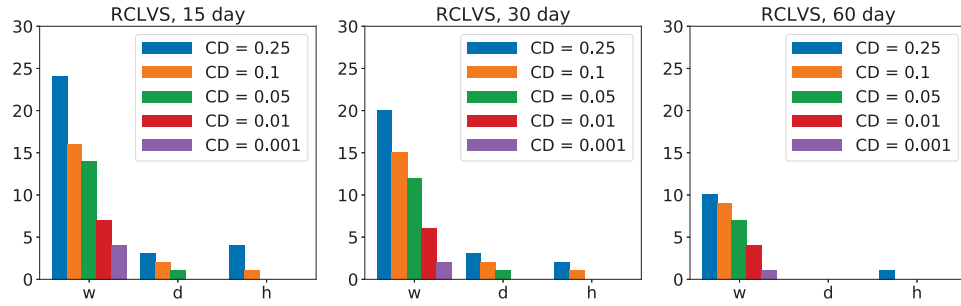
Figure 11: Number of RCLVs detected in the domain for the different 2D experiments (h - hourly, d - daily, w - weekly) at different times for different choices of convexity deficiency (CD).
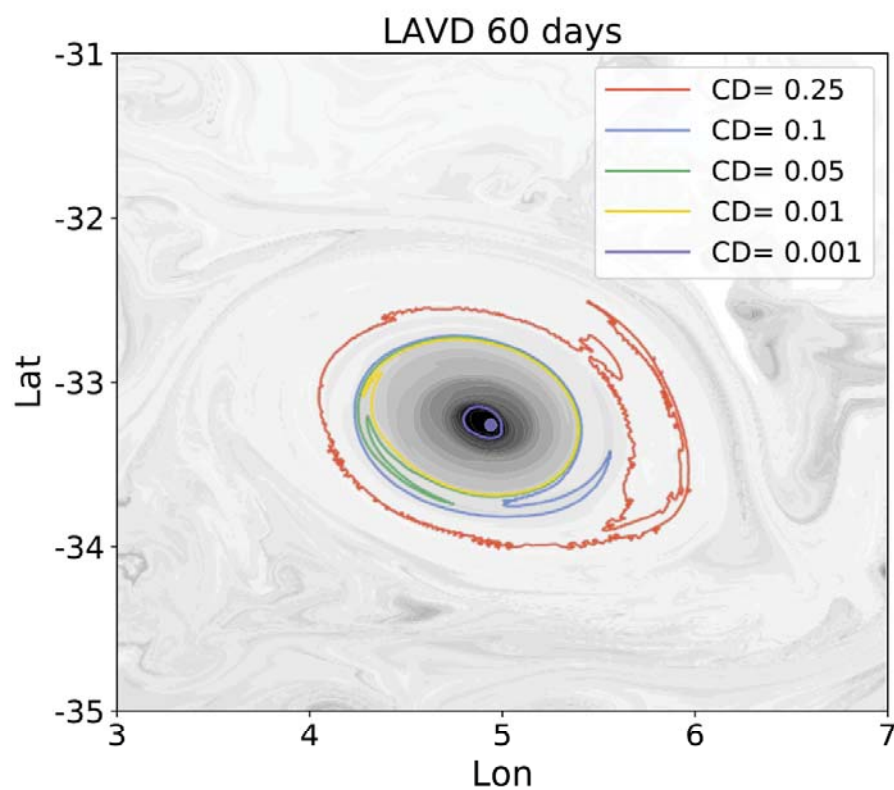
Figure 12: Closed convex contours of LAVD in 2D-w for different choices of CD overlaid on the 60 day LAVD field in Gray.
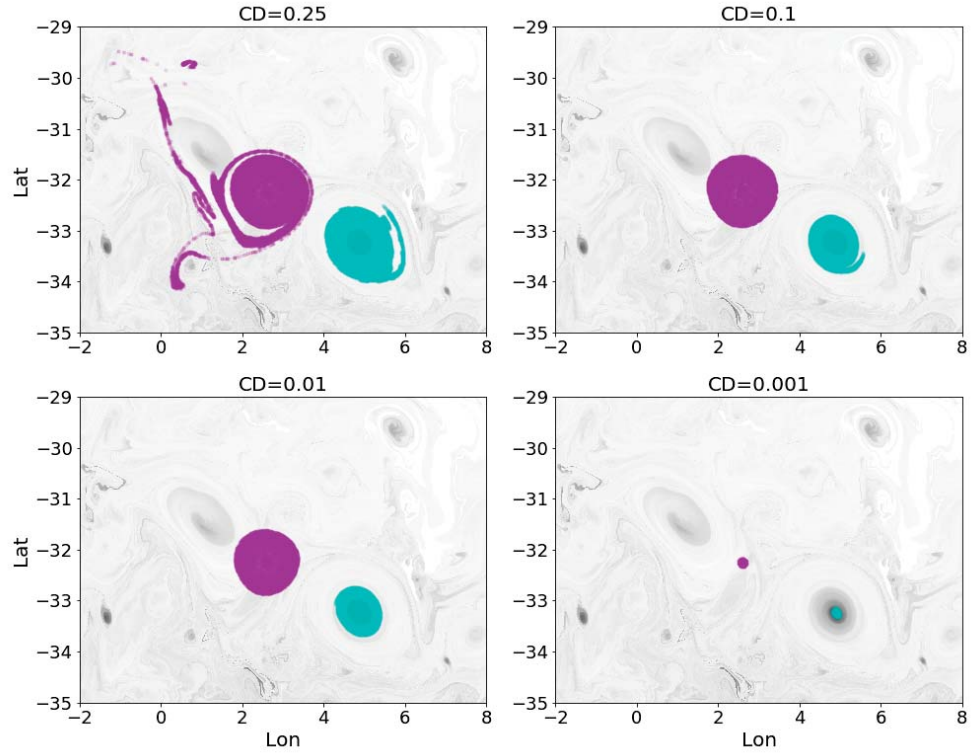
Figure 13: Trajectories of particles over 60 days inside an RCLV (identified from closed convex contours of LAVD in 2D-w) for different choices of CD overlaid on the 60 day LAVD contours in Gray. The cyan circles represent the initial positions and the magenta ones are the final positions.
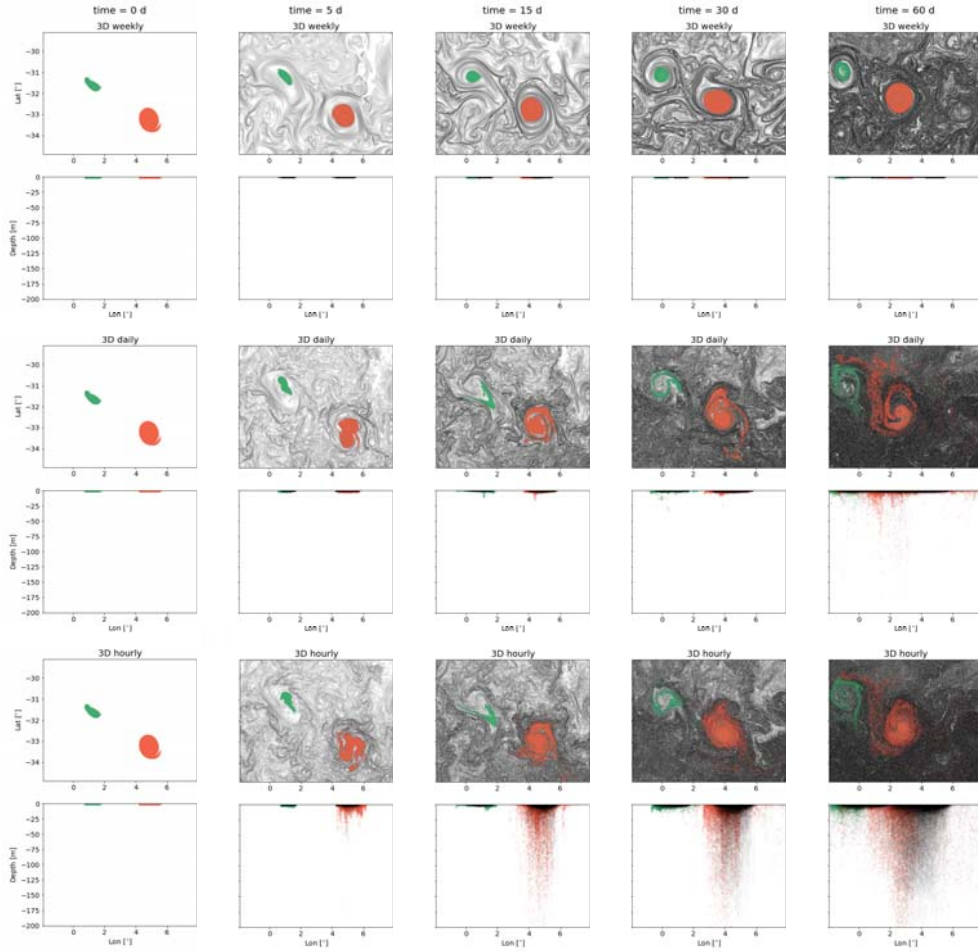
Figure 14: Snapshots at 0, 5, 15, 30, and 60 days showing the evolution of two different RCLVs (represented by the red and green dots) detected from closed convex contours (CD=0.1) of LAVD in 3D-w (top), in the horizontal and vertical directions. The middle and bottom two rows show the trajectories of the same particles (with the same initial positions) in 3D-d and 3D-h respectively. The grayscale background in the horizontal represents the backward time FTLE mapped on to the particle positions at each time. In the vertical, the particle trajectories for every 10th particle is shown in gray. (See Supplementary Information for animations.)
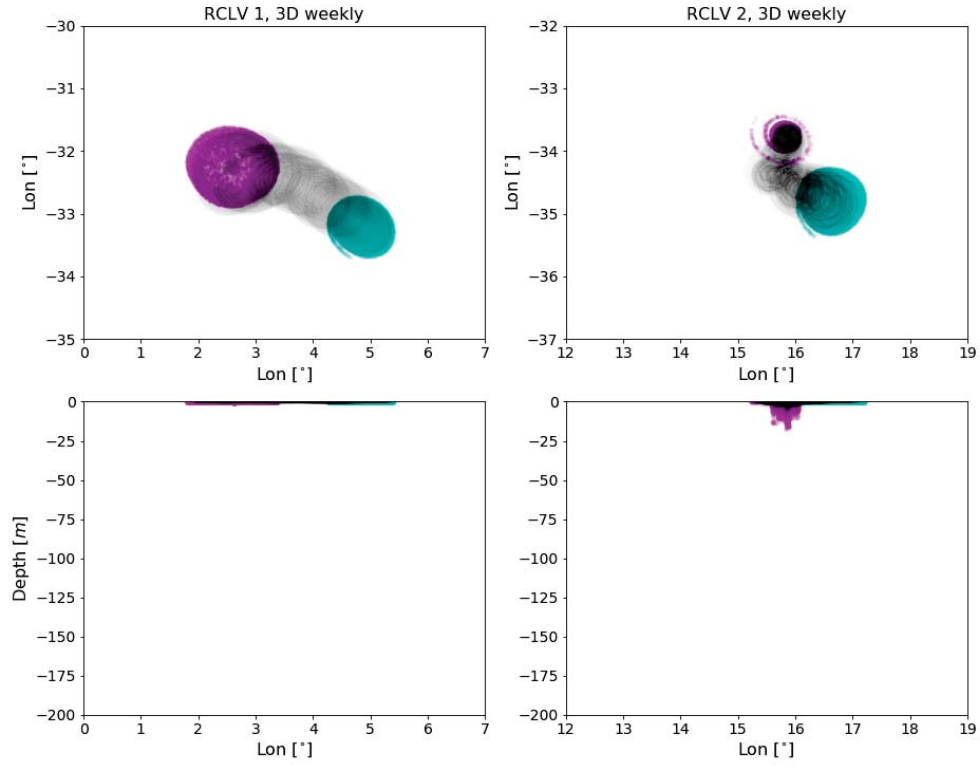
Figure 15: Trajectories of particles inside three different kinds of RCLVs identified from the closed convex contours (CD=0.1) of LAVD in 3D-w experiments : An expanding eddy (left), a nd a shrinking eddy (right). The cyan dots represent the initial positions and the magenta dots represent the positions reached by the particles after 60 days . The trajectories for every 10th particle is shown in gray.
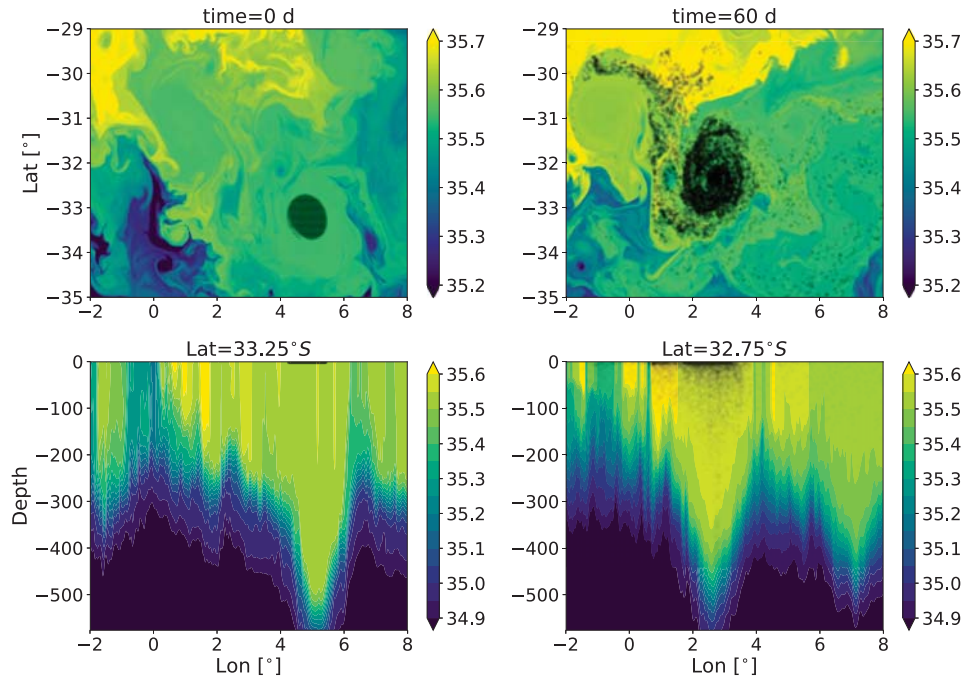
Figure 16: An expanding RCLV: Snapshots of the initial (left) and final (right) positions of 3D particles with the same initial positions as RCLV 1 (left column of Fig. 15) advected offline by hourly velocities superimposed on salinity concentration in the region from online llc4320 simulation output. The colors in the top panels show the salinity at the surface. The bottom panels show a cross section (taken along a latitude line, across the eddy) of the salinity field and the particles are shown in black. The cross section of salinity at different times show clear upwelling inside the eddy core.
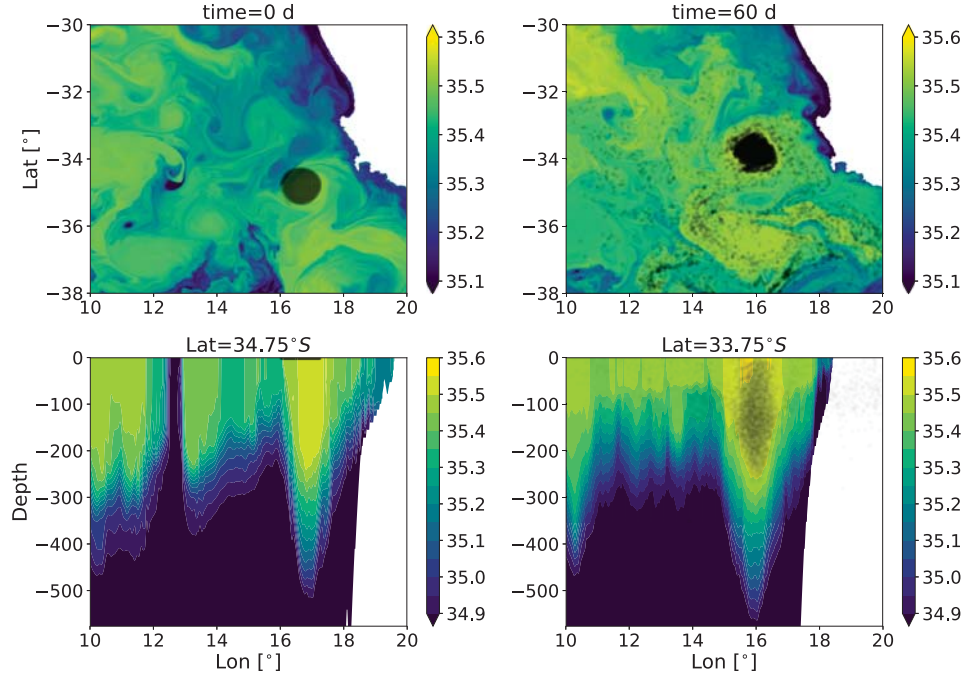
Figure 17: A shrinking RCLV: Snapshots of the initial (left) and final (right) positions of 3D particles with the same initial positions as RCLV 2 (middle column of Fig. 15) advected offline by hourly velocities superimposed on salinity concentration in the region from online llc4320 simulation output. The colors in the top panels show the salinity at the surface. The bottom panels show a cross section (taken along a latitude line, across the eddy) of the salinity field and the particles are shown in black. The salinity at depth inside the eddy is higher at 60 days indicating that there is downwelling inside the eddy core.
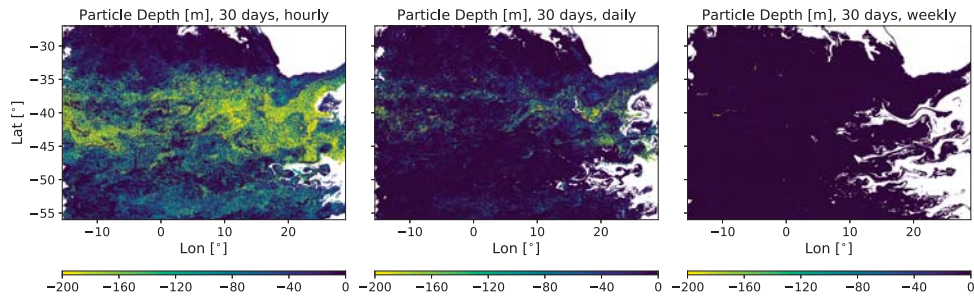

Figure 18: Depth after 30 days, for Lagrangian particles in the Agulhas sector advected by (a) Hourly velocities, (b) Daily averaged velocities, and (c) Weekly averaged velocities from the llc4320 numerical model simulations. The mask (white) represents the initial positions of all particles that reached the edge of the domain at the end of the integration.
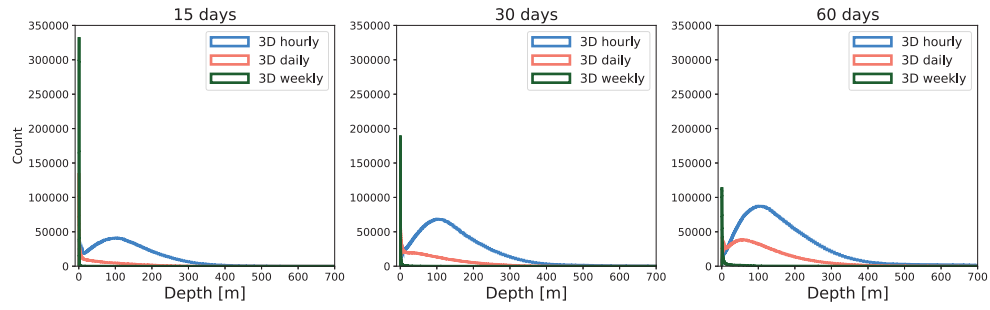
Figure 19: Histogram showing the pdf of particle depth after 15 days (left), 30 days (middle) and 60 days (right) for all the 3D particle advection simulations.